

Molecular hydrogen emission from protoplanetary disks[★]

H. Nomura^{★★} and T. J. Millar

School of Physics and Astronomy, The University of Manchester, PO Box 88, Manchester M60 1QD, UK
e-mail: hnomura@kobe-u.ac.jp

Received 3 February 2005 / Accepted 21 April 2005

Abstract. We have modeled self-consistently the density and temperature profiles of gas and dust in protoplanetary disks, taking into account irradiation from a central star. Making use of this physical structure, we have calculated the level populations of molecular hydrogen and the line emission from the disks. As a result, we can reproduce the observed strong line spectra of molecular hydrogen from protoplanetary disks, both in the ultraviolet (UV) and the near-infrared, but only if the central star has a strong UV excess radiation.

Key words. line: formation – molecular processes – radiative transfer – planetary systems: protoplanetary disks

1. Introduction

It has long been believed that infrared excesses over the stellar photospheric emissions, often observed in the spectral energy distributions of young stellar objects (YSOs), arise from dusty circumstellar disks (Cohen 1974; Kenyon & Hartmann 1987; Beckwith & Sargent 1993). More direct evidence for circumstellar disks has been found recently in the form of optically thick dust lanes against the scattered light of the surrounding optically thin nebulae at optical and near-infrared wavelengths (e.g., Burrows et al. 1996; Stapelfeldt et al. 1998, 2003; Cotera et al. 2001; Jayawardhana et al. 2002) and as a near-infrared image of the scattered light of the disk itself (e.g., Fukagawa et al. 2004).

Furthermore, thanks to recent high spectral resolution and high sensitivity observations, it has become possible to detect various molecular line emission from protoplanetary disks (e.g., Dutrey et al. 1997). In particular, observation of molecular hydrogen line emission from the disks is important because it directly traces gaseous masses of the disks, which are connected with giant planet formation, without assuming the dust-to-gas ratio or CO-to-H₂ ratio. Pure rotational molecular hydrogen line emission was detected towards YSOs and debris-disk objects with the *Infrared Space Observatory (ISO)* (Thi et al. 1999, 2001a,b), while no emission has yet been observed with ground-based telescopes (Richter et al. 2002; Sheret et al. 2003; Sako et al. 2005). Ro-vibrational molecular hydrogen line emission with narrow line widths was detected towards some T Tauri stars (Weintraub et al. 2000;

Bary et al. 2002, 2003; Itoh et al. 2003). In addition, fluorescent molecular hydrogen line emission in the ultraviolet (UV) wavelength band was observed towards some classical T Tauri stars (Herczeg et al. 2002, 2004; Bergin et al. 2004). However, at present there is no established model for this emission which takes into account the global physical structure of protoplanetary disks.

Historically, molecular hydrogen emission has been observed towards various kinds of astronomical objects, such as shock surfaces associated with star forming regions, reflection nebulae illuminated by nearby massive stars, planetary nebulae, supernova remnants, external galaxies, etc. (e.g., Beckwith et al. 1978; Brown et al. 1983; Hasegawa et al. 1987; Burton et al. 1992), and studied theoretically, for example, under the conditions of shock or photon-dominated regions (e.g., Black & Dalgarno 1976; Shull 1978; Hollenbach & McKee 1979; Draine et al. 1983; Pineau des Forets et al. 1986; Black & van Dishoeck 1987; Wagenblast & Hartquist 1988; Sternberg 1988, 1989; Sternberg & Dalgarno 1989; Draine & Bertoldi 1996). These studies have suggested the importance of physical condition of the objects – density, temperature, and UV irradiation – for exciting molecular hydrogen.

Now, the physical structure of protoplanetary disks is thought to be controlled by irradiation from the central star. Modelling the density and temperature profiles of dust and gas in the disks has been developed in more and more realistic ways as more detailed observational data become available (e.g., Kusaka et al. 1970; Kenyon & Hartmann 1987; Chiang & Goldreich 1997; D’Alessio et al. 1998; Nomura 2002; Dullemond et al. 2002; Dullemond & Dominik 2004; Kamp & van Zeldelhoff 2001; Gorti & Hollenbach 2004; Glassgold et al. 2004; Kamp & Dullemond 2004; Jonkheid et al. 2004).

[★] Appendices A, B, C, and D are only available in electronic form at <http://www.edpsciences.org>

^{★★} Now at Department of Earth & Planetary Sciences, Graduate School of Science and Technology, Kobe University, Kobe 657-8501, Japan.

In this paper, we have modeled the density and temperature profiles of protoplanetary disks self-consistently, taking into account the irradiation from the central T Tauri star. We have used these to investigate the abundance and excitation of molecular hydrogen in the disk, and the observational properties of the molecular hydrogen emission from the disk. In the following section, we present the physical model of the disk: the density and temperature profiles of the gas and dust in the disk on the assumptions of vertical hydrostatic equilibrium and local thermal and radiative equilibrium. In Sect. 3, we calculate the abundance and level populations of molecular hydrogen, assuming statistical equilibrium among the levels. Making use of these physical and chemical profiles, we compute molecular hydrogen emission from the disk at infrared and ultraviolet wavelengths and compare with the observations in Sect. 4. Finally, the results are summarized in Sect. 5.

2. Physical model

We consider an axisymmetric disk surrounding a central star with the physical parameters of typical T Tauri stars; a mass of $M_* = 0.5 M_\odot$, a radius of $R_* = 2 R_\odot$, and a temperature of $T_* = 4000$ K (e.g., Kenyon & Hartmann 1995).

2.1. Basic equations for the disk structure

The gas temperature and density distributions of the disk are obtained self-consistently by iteratively solving the equations for hydrostatic equilibrium in the vertical direction and local thermal balance between heating and cooling of gas. The equation for vertical hydrostatic equilibrium is given in cylindrical coordinates (x, z) by

$$\frac{dP}{dz} = c_s^2 \frac{d\rho}{dz} = -\rho g_z, \quad (1)$$

where P and ρ represent the pressure and density, respectively. The sound speed c_s is defined as $c_s^2 \equiv dP/d\rho = kT/m_\mu$, where k and T represent Boltzmann's constant and the gas temperature, and the mean molecular mass m_μ is set to be $m_\mu = 2.3m_H$ (m_H is the hydrogen mass). The vertical gravitational force is set $g_z = GM_*/(x^2 + z^2)^{3/2}$, where G is the gravitational constant. The condition, $\int_{z=-\infty}^{\infty} \rho(x, z) dz = \Sigma(x)$, is set to be satisfied, where $\Sigma(x)$ is the surface density at a radius x defined below. We put $\rho(x, z_\infty) = 1.67 \times 10^{-20}$ g cm $^{-3}$ for the boundary condition. The equation for the detailed energy balance at each point in the disk is given by

$$\Gamma = \Lambda, \quad (2)$$

where Γ and Λ are the sum of the relevant gas heating and cooling rates, respectively (see Appendix A for details of the heating and cooling processes).

The dust temperature profile plays an important role in determining the disk structure because the gas temperature is well coupled with the dust temperature near the midplane of the disks where the density is high enough for efficient collisions between gas and dust particles (see Sect. 2.4). In this paper we obtain the dust temperature profile by assuming local radiative equilibrium between absorption and reemission of

radiation by dust grains at each point in the disk in spherical coordinates (R, Θ) ,

$$4\pi \int_0^\infty d\nu \kappa_\nu(R, \Theta) B_\nu[T_d(R, \Theta)] \\ = \int_0^\infty d\nu \kappa_\nu(R, \Theta) \oint d\mu d\phi I_\nu(R, \Theta; \mu, \phi), \quad (3)$$

where κ_ν , I_ν , $B_\nu(T_d)$, and T_d represent the monochromatic absorption coefficient, the specific intensity, the Planck function for blackbody radiation at a frequency ν , and the dust temperature, respectively. Local thermodynamic equilibrium, $\eta_\nu = \kappa_\nu B_\nu(T_d)$, is assumed, where η_ν is the monochromatic emissivity. The specific intensity is calculated by solving the axisymmetric two-dimensional radiative transfer equation,

$$I_\nu(R, \Theta; \mu, \phi) = \int_0^S \kappa_\nu(R', \Theta') \rho(R', \Theta') \\ \times B_\nu[T_d(R', \Theta')] e^{-\tau_\nu(R', \Theta')} ds', \quad (4)$$

where $\tau_\nu(R', \Theta')$ is the specific optical depth from a point (R', Θ') to (R, Θ) , by means of the short characteristic method in spherical coordinates (Dullemond & Turolla 2000). Here we neglect the effect of scattered light (cf. Dullemond & Natta 2003). As heating sources we consider the radiative flux produced by the viscous dissipation (α -model) at the midplane of the disk, $F_{\text{vis}} = (9/4)\Sigma\alpha c_{s0}^2\Omega$, and the irradiation from the central star $F_{\nu, \text{star}}$ (Appendix C; see also Nomura 2002 for details of the model).

The surface density distribution of the disks, $\Sigma(x)$, is determined based on the standard accretion disk model (e.g., Lynden-Bell & Pringle 1974; Pringle 1981), by equating the gravitational energy release of accreting mass to thermal heating via viscous dissipation at the disk midplane at each radius, x ,

$$\frac{9}{4}\Sigma\alpha c_{s0}^2\Omega = \frac{3GM_*\dot{M}}{8\pi x^3} \left[1 - \left(\frac{R_*}{x} \right)^{1/2} \right], \quad (5)$$

where c_{s0} and $\Omega = (GM_*/x^3)^{1/2}$ represent the sound speed at the midplane and the Keplerian frequency, respectively. Here, we adopt $\alpha = 0.01$ for a viscous parameter, and assume that the disk has a constant mass accretion rate of $\dot{M} = 10^{-8} M_\odot \text{ yr}^{-1}$. The disk mass between the inner radius $r_{\text{in}} = R_* = 2 R_\odot$ and the outer radius $r_{\text{out}} = 100$ AU is then $6 \times 10^{-3} M_\odot$.

2.2. Ultraviolet radiation fields

Ultraviolet (UV) radiation fields affect the gas temperature of the protoplanetary disks through the grain photoelectric heating (Appendix A.1) as well as the photodissociation and photoionization processes (Appendix B and Sect. 3).

The main UV radiation sources are generally thought to be due to the central star and the interstellar radiation field. In this paper we simply adopt a 1+1 dimensional UV radiation field. In the radial direction, we calculate the radiation field which directly comes from the central star as

$$F_{\nu, R}(R, \Theta) = f F_{\nu, \text{star}} \exp(-\tau_{\nu, R}), \quad \tau_{\nu, R} = \int_{R_*}^R \chi_\nu \rho dR, \quad (6)$$

where $F_{v,\text{star}}$ is the specific radiation field at the stellar surface, $f = (\pi/4)(R_*/R)^2$ the reduction of radiation by a geometrical effect. $\tau_{v,R}$ is the specific optical depth from the stellar surface (R_*, Θ) to a point (R, Θ), and χ_v is the monochromatic extinction coefficient defined by the absorption (κ_v) and scattering (σ_v) coefficients as $\chi_v \equiv \kappa_v + \sigma_v$. In the vertical direction, we consider the radiation source of the interstellar radiation field, $F_{v,\text{ISRF}}$, plus the contribution of the scattering of radiation from the central star,

$$F_{v,z}(x, z) = F_{v,\text{ISRF}} \exp[-\tau_{v,z}(z_\infty)] + 2\pi\omega_v \int_z^{z_\infty} \kappa_v(x, z') \rho(x, z') F_{v,R}(x, z') e^{-\tau_{v,z}(z')} dz',$$

$$\tau_{v,z}(z') = \int_z^{z'} \chi_v \rho dz'', \quad (7)$$

where ω_v is the monochromatic albedo defined by the absorption and extinction coefficients as $\omega_v \equiv \sigma_v/\chi_v$, and $\tau_{v,z}(z')$ is the specific optical depth from a point (x, z) to (x, z'). The approximate treatment of the scattered light in this model could overestimate the UV radiation fields in the disks. Fully two-dimensional radiative transfer calculation including the scattering process should be done in future (e.g., van Zadelhoff et al. 2003).

Now, it is known observationally that many classical T Tauri stars have excess continuum radiation in the ultraviolet region, compared to the main-sequence stars of similar effective temperature (e.g., Herbig & Goodrich 1986; Herbst et al. 1994; Valenti et al. 2000). The UV excess radiation is considered to result from the shock on the stellar surface which is caused by a magnetospheric accretion flow from the accretion disk onto the star (e.g., Calvet & Gullbring 1998; Ostriker & Shu 1995). In order to examine the effects of this UV excess radiation on the disk structure and the H_2 line emission from the disk, we treat two kinds of models for radiation from the central star, $F_{v,\text{star}}$: models with and without UV excess. In the model with UV excess, $F_{v,\text{star}}$ consists of three components: black body emission at the star's effective temperature, T_* , an optically thin hydrogenic thermal bremsstrahlung emission at a higher temperature, and Ly α line emission, based on observations towards TW Hydrae (see Appendix C). In the model without UV excess, the stellar radiation is assumed to be black body emission only.

For the interstellar radiation field, $F_{v,\text{ISRF}}$, we adopt the Draine (1978) field for the wavelength range of $912 \text{ \AA} < \lambda < 2000 \text{ \AA}$ and the field given by van Dishoeck & Black (1982) for $\lambda > 2000 \text{ \AA}$.

2.3. Dust model

The physical and chemical structure of protoplanetary disks is affected by the dust model in various ways: first, it affects the radiation field because dust grains are the dominant opacity source in protoplanetary disks. Thus, the dust temperature profile is influenced by the dust model through the absorption (κ_v) and extinction (χ_v) coefficients (Sect. 2.1). Also, it affects the UV radiation field (through the extinction coefficient χ_v and albedo ω_v ; Sect. 2.2), that is, the photodissociation and

photoionization processes (see Appendix B and Sect. 3). The gas temperature profile is also affected because grain photoelectric heating induced by UV photons is the dominant source of gas heating at the disk surface (see Appendix A.1 and Sect. 2.4) and by grain-gas collisions (see Appendix A.2). Second, the total surface area of the dust grains affect the molecular hydrogen abundance through the H_2 formation rate on grain surfaces (Sect. 3).

In this paper we assume that the dust particles consist of silicate, carbonaceous grains, and water ice, and have size distributions obtained by Weingartner & Draine (2001a, hereafter WD01a) which reproduce the observational extinction curve of dense clouds (see Appendix D for details). Also, the dust and gas are assumed to be well-mixed.

2.4. Resulting temperature and density profiles

We obtain self-consistent density and temperature distributions of a protoplanetary disk by solving the equations for vertical hydrostatic equilibrium and local thermal balance between heating and cooling of gas iteratively together with the local radiative equilibrium equations on dust grains (see Sect. 2.1). Figure 1a shows the contour plots of the resulting temperature (a-1) and density (a-2) profiles in the $x - z$ plane. The contour levels are $T = 30, 100, 300,$ and 1000 K for the temperature, and $\rho = 10^{-20}, 10^{-18}, 10^{-16}, 10^{-14},$ and $10^{-12} \text{ g cm}^{-3}$ for the density. In order to see the effects of the UV excess radiation, we also calculate for comparison the structure of the disk which is irradiated by stellar radiation without UV excess (Fig. 1b; see Sect. 2.2).

Figure 2 shows the corresponding gas (solid lines) and dust (dotted lines) temperature profiles in the vertical direction at the radii of $x = 1, 10$ and 100 AU (a-1) (b-1). The horizontal axis is the vertical height divided by each radius. The gas temperature profiles as a function of the distance from the central star, $R = (x^2 + z^2)^{1/2}$, are also plotted in (a-2) and (b-2) for $z/x = 0.0, 0.1, 0.2, 0.4,$ and 0.8 . The figures show that in the model with UV excess radiation the gas temperature at the disk surface is much higher than the dust temperature and reaches around 1000 K even at the radius of 10 AU . This is due to the grain photoelectric heating induced by the strong far ultraviolet (FUV) radiation from the central star. On the other hand, near the midplane of the disk and at the outer disk in the model without UV excess, where the UV radiation field is not strong enough to heat up the gas, the gas temperature is close the dust temperature due to the collisions between the gas and dust particles (see below). We calculate the gas temperature only in the upper region of the disk where the difference between the gas and dust temperatures are more than 1% ($|T - T_{\text{d}}|/T > 10^{-2}$), considering that the gas temperature is almost the same as the dust temperature near the midplane. The gas temperature in ionized region is assumed to be $T = 10^4 \text{ K}$ (see Appendix B.1). Now, the corresponding vertical (1) and radial (2) density profiles of the disk in the models with (solid lines) and without (dotted lines) UV excess radiation are plotted in Fig. 3. The strong UV radiation field at the disk surface heats the gas hot enough to make the disk expand in the vertical direction.

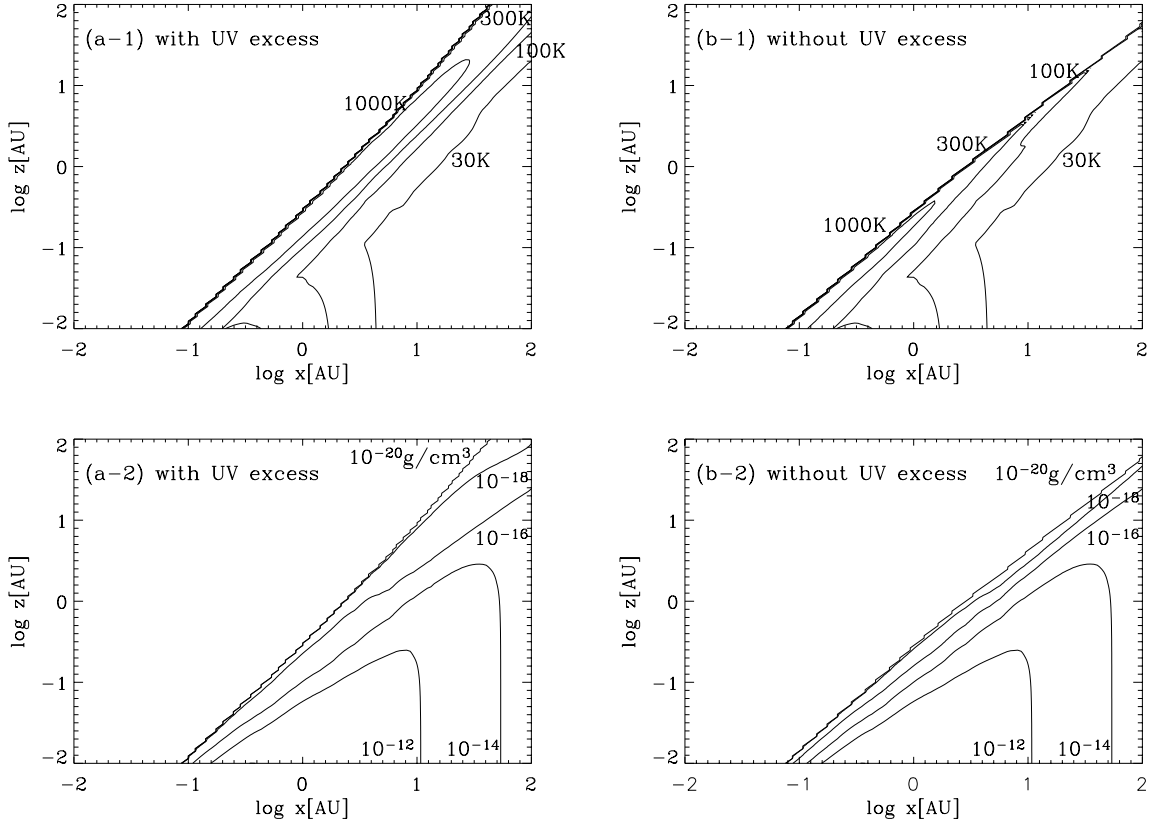


Fig. 1. The gas temperature (a-1) (b-1) and density (a-2) (b-2) distributions in the $x - z$ plane for the models **a**) with and **b**) without UV excess radiation of the central star.

Therefore, the higher density at the disk surface in the model with UV excess radiation is caused by the stronger UV radiation fields.

The integrated FUV radiation fields ($6 \text{ eV} < h\nu < 13 \text{ eV}$) in the disk for the models with and without UV excess radiation are shown in Fig. 4. The radial (dashed lines), $G_{\text{FUV},R}$, and vertical (dotted lines), $G_{\text{FUV},z}$, fields are calculated by integrating the specific radiation field $F_{\nu,R}$ (Eq. (6)) and $F_{\nu,z}$ (Eq. (7)), respectively, in the FUV region ($6 \text{ eV} < h\nu < 13 \text{ eV}$). The total radiation fields (solid lines) are summations of the radial and vertical fields, $G_{\text{FUV}} = G_{\text{FUV},R} + G_{\text{FUV},z}$. The figures show that the direct irradiation from the central star dominates the radiation field in the upper layer, while the scattered field is superior in the lower layer (see also van Zadelhoff et al. 2003; Bergin et al. 2003). The contribution of the interstellar radiation field (dot-dashed lines), $G_{\text{FUV,ISRF}} = \int F_{\nu,\text{ISRF}} \exp[-\tau_{\nu,z}(z_{\infty})] d\nu$, is also plotted in this figure, which shows that it is not dominant except in the lower layer of the outer region ($x \sim 100 \text{ AU}$) in the model without UV excess radiation.

The vertical profiles of the heating and cooling rates at the radii of (a) 10 AU and (b) 100 AU for the model with UV excess radiation are plotted in Fig. 5. We can see from the figure that the dominant heating source is grain photoelectric heating in the region where we calculate the gas temperature ($|T - T_{\text{d}}|/T > 10^{-2}$). Meanwhile, the energy transfer from gas to dust particles via collisions is the dominant cooling source at the inner region and near the midplane of the disk where the matter is dense

enough, while radiative cooling via line transition is dominant in less dense region.

3. Abundance and excitation of H_2

3.1. The model

The abundance and the level populations of the $X^1\Sigma_g^-$ electronic state of molecular hydrogen in a statistical equilibrium state are calculated based on Wagenblast & Hartquist (1988) as

$$n_l(\text{H}_2) \left[\sum_{m \neq l} \left(A_{lm} + \beta_{lm} + \sum_s n_s C_{lm}^s \right) + R_{\text{diss},l} \right] + k_{\text{O}+\text{H}_2} n(\text{O}) n_l(\text{H}_2) = \sum_{m \neq l} n_m(\text{H}_2) \left(A_{ml} + \beta_{ml} + \sum_s n_s C_{ml}^s \right) + n(\text{H}) R_{\text{form},l} \quad (8)$$

where A_{lm} is the Einstein A-coefficient for spontaneous emission from level l to level m ($A_{lm} = 0$ if the energy of level l , E_l , is smaller than E_m) and C_{lm}^s is the collisional transition rate with collision partner s . The collisional rate coefficients are taken from Smith et al. (1982) and Black & Dalgarno (1977) for collisions with H^+ , Tiné et al. (1997; see also references therein) for the collisions with H_2 , and Lepp et al. (1995; see also Tiné et al. 1997) for the collisions with H (<http://www.physics.unlv.edu/astrophysics/>).

The symbol β_{lm} in Eq. (8) represents the effective rate for transition $l \rightarrow m$ via ultraviolet pumping followed by radiative

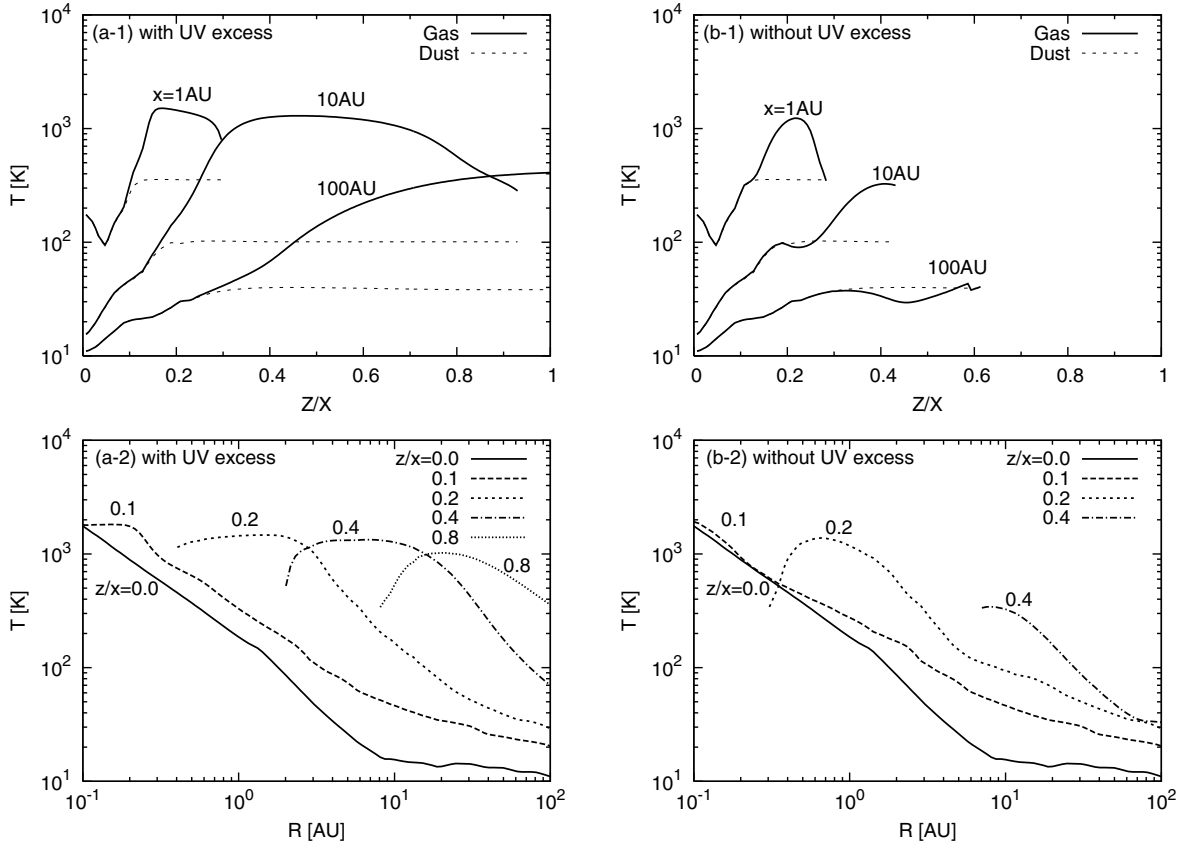


Fig. 2. The vertical temperature profiles of gas (solid lines) and dust (dotted lines) at the disk radii of $x = 1, 10$ and 100 AU (a-1) (b-1), and the radial temperature profiles of gas at $z/x = 0.0, 0.1, 0.2, 0.4$, and 0.8 (a-2) (b-2) for the models **a)** with and **b)** without UV excess. In the model **a)** the gas temperature at the disk surface can reach around 1000 K due to the grain photoelectric heating, while it is almost the same as the dust temperature near the midplane.

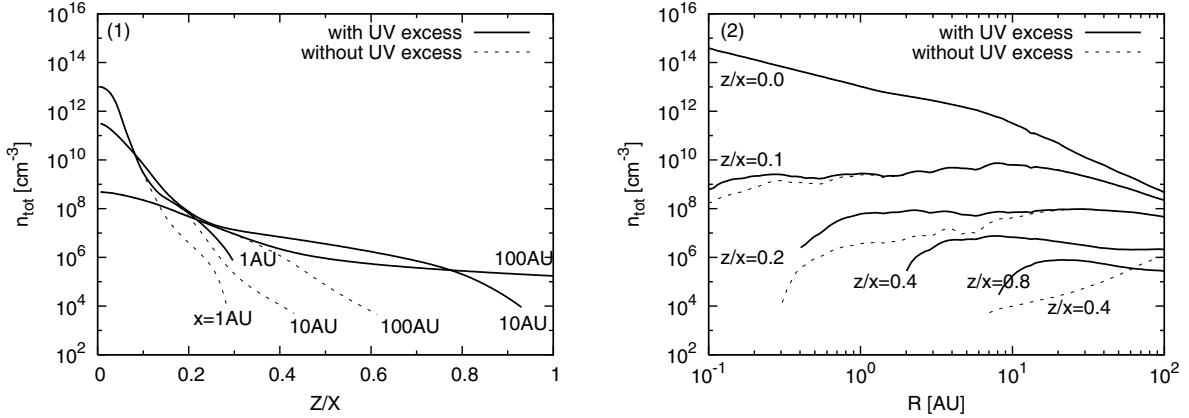


Fig. 3. The vertical gas density profiles at the disk radii of $x = 1, 10$ and 100 AU **1)**, and the radial gas density profiles at $z/x = 0.0, 0.1, 0.2, 0.4$, and 0.8 **2)** for the models with (solid lines) and without (dotted lines) UV excess. The UV irradiation heats the gas and makes the disk expand vertically, which results in higher density at the disk surface.

cascades and $R_{\text{diss},l}$ is the photodissociation rates of hydrogen molecules in level l . The UV radiation fields are calculated as discussed in Sect. 2.2. An approximate function given by Federman et al. (1979) is used for the H_2 self-shielding of the UV radiation fields. A purely thermal Doppler widths of $v_d = (2kT/m_\mu)^{0.5}$ is adopted in this function. Molecular hydrogen excitation due to X-ray induced electron impact should be taken into account in future (e.g., Bergin et al. 2004).

The symbol $R_{\text{form},l}$ represents the effective formation rate of H_2 in level l on grain surfaces. The molecular hydrogen which leaves the grain surfaces is assumed to originate in the levels ($v = 7, J = 1$) and ($v = 7, J = 0$) with the ratio of 9:1 and cascade into the level l , following Duley & Williams (1986) (cf. Takahashi & Uehara 2001 for new formation pumping model). The total formation rate of $\sum_l R_{\text{form},l} = 7.5 \times 10^{-18} T^{0.5} \epsilon_{\text{H}_2} n_{\text{tot}} n(\text{H}) \text{ cm}^{-3} \text{ s}^{-1}$ is adopted

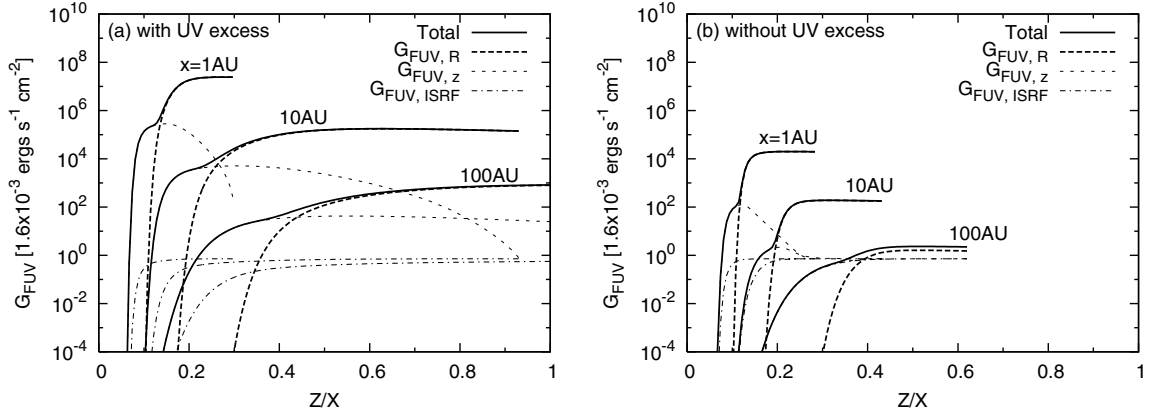


Fig. 4. The integrated FUV radiation fields ($6 \text{ eV} < h\nu < 13 \text{ eV}$) as a function of the vertical height of the disk at the radii of $x = 1, 10$ and 100 AU for the models **a**) with and **b**) without UV excess. The solid, dashed and dotted lines show the total, radial, and vertical radiation fields, respectively. The contributions of the interstellar radiation fields are plotted in the dot-dashed lines.

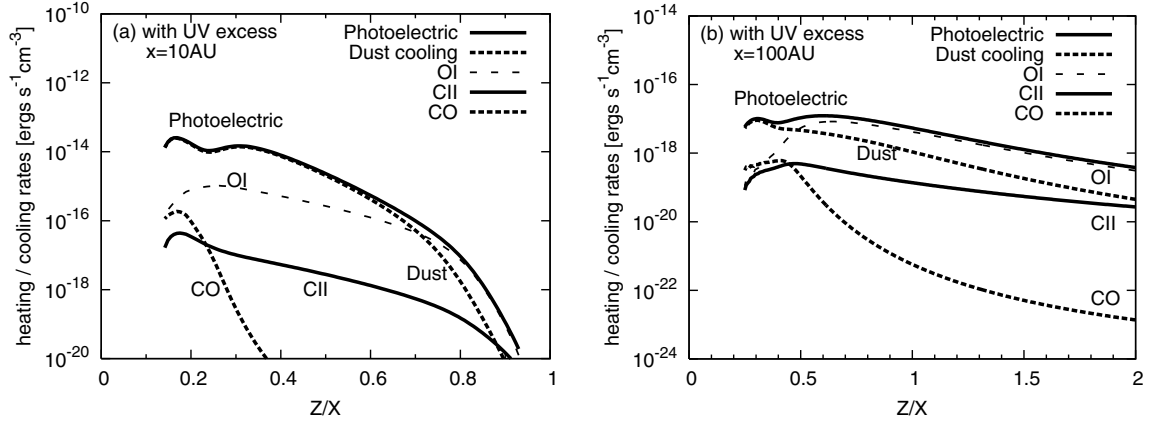


Fig. 5. The vertical cooling and heating rates at the disk radii of **a**) $x = 10 \text{ AU}$ and **b**) 100 AU for the models with UV excess. The grain photoelectric heating dominates the heating process, while the gas–grain collisions and the radiative cooling dominate the cooling process in the dense and less dense regions, respectively.

here. The symbol ϵ_{H_2} represents the recombination efficiency of atomic hydrogen on dust grains which is estimated by Cazaux & Tielens (2002, 2004) based on laboratory experiments (e.g., Pirronello et al. 1999; Zecho et al. 2002).

The endothermic reaction $\text{O} + \text{H}_2 \rightarrow \text{OH} + \text{H}$, which dominates the destruction of molecular hydrogen in high temperature regions (e.g., Storzer & Hollenbach 1998), is also taken into account. The reaction rate coefficient of $k_{\text{O}+\text{H}_2} = 3.14 \times 10^{-13} (T/300 \text{ K}) \exp(-3150 \text{ K}/T) \text{ cm}^3 \text{ s}^{-1}$ is adopted from the UMIST RATE99 database (Le Teuff et al. 2000).

The total number density of hydrogen nuclei at each point in the disk is required to satisfy the condition,

$$n_{\text{tot}} = n(\text{H}) + 2n(\text{H}_2) + n(\text{H}^+) + 2n(\text{H}_2^+) + 3n(\text{H}_3^+), \quad (9)$$

where $n(s)$ represents the number density of species s . A simple chemical equilibrium scheme given in Wagenblast & Hartquist (1988) is used to obtain the number densities of the related species.

3.2. Results

The resulting molecular (solid lines) and atomic (dashed lines) hydrogen abundances in the vertical direction at the radii of $x = 1, 10$ and 100 AU are plotted in Fig. 6. Molecular hydrogen is photodissociated at the very surface of the disk, while it is destroyed by atomic oxygen where the gas temperature is $\sim 1000 \text{ K}$.

Figure 7 shows the resulting level populations of molecular hydrogen. The filled diamonds, open squares, and asterisks show the column densities of molecular hydrogen in each ro-vibrational level as a function of the level energy at each radius of 1, 10 and 100 AU, respectively. The column densities are calculated by integrating the number density of molecular hydrogen in each level along the vertical direction at each radius of the disk. The level populations in local thermodynamic equilibrium (LTE) at each radius are shown in the dashed lines. Also, we present the level populations in the model without UV excess in Fig. 7b for comparison. Figures labeled (1), (2), and (3) show the level populations at the radius of 1 AU, 10 AU, and 100 AU, respectively, and they are plotted together in figure (0) for comparison. We can see from the figures that if the

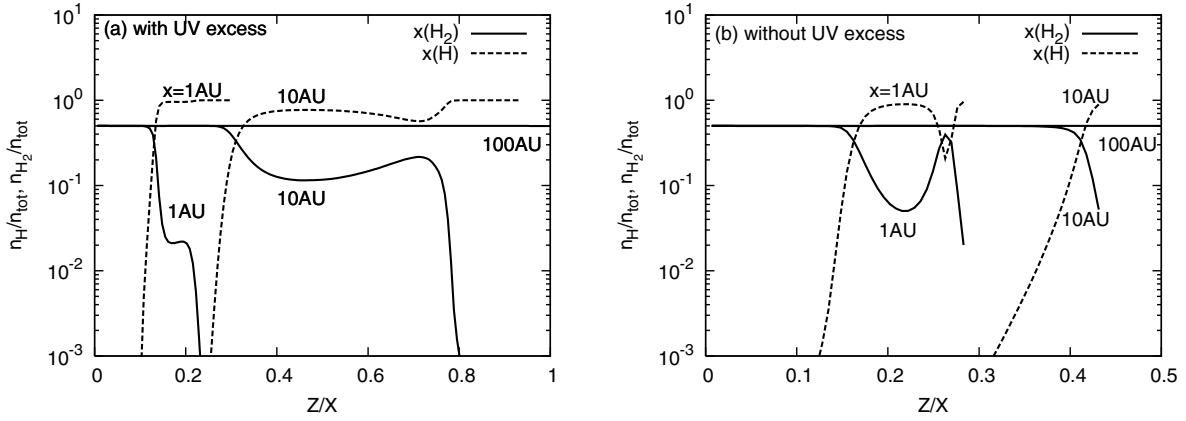


Fig. 6. The vertical molecular (solid lines) and atomic (dashed lines) hydrogen abundances at the disk radii of $x = 1, 10$ and 100 AU for the models **a)** with and **b)** without UV excess radiation. The molecular hydrogen is photodissociated at the very disk surface and destroyed by atomic oxygen where the gas temperature is ~ 1000 K.

central star has a UV excess, the gas becomes hot enough, as we have seen in the previous section, that the collisional processes are very efficient and the level populations are in LTE except for those of the very high levels. And as a result of the high temperature, the populations of the upper levels become very large. On the other hand, in the outer disk in the model without UV excess where the gas is cold enough, the level populations are not in LTE but are affected by the UV pumping process. Also we can see that in this model, the populations of the upper levels are not as large as those in the model with UV excess.

4. Molecular hydrogen emission

Making use of the level populations we obtained in Sect. 3, we calculate the molecular hydrogen emission from the disk. The intensity of each line integrated over the frequency, I_{ul} , is obtained by solving the radiative transfer equation in the vertical direction of the disk, assuming that an observer faces the disk,

$$\frac{dI_{ul}}{dz} = -\chi_{ul}(I_{ul} - S_{ul}), \quad (10)$$

where the subscripts ul means the transition from the upper to the lower levels. The source function, S_{ul} , and the total extinction coefficient, χ_{ul} , are given as

$$S_{ul} = \frac{1}{\chi_{ul}} n_u A_{ul} \Phi_{ul} \frac{h\nu_{ul}}{4\pi} \quad (11)$$

and

$$\chi_{ul} = \rho \chi_{\nu_{ul}} + (n_l B_{lu} - n_u B_{ul}) \Phi_{ul} \frac{h\nu_{ul}}{4\pi}, \quad (12)$$

where the symbols A_{ul} and B_{ul} are the Einstein coefficients for the transition $u \rightarrow l$, and n_u and n_l are the number densities of the upper and lower levels, respectively. The energy difference between the levels u and l corresponds to $h\nu_{ul}$. The symbol Φ_{ul} is the line profile function, ρ the gas density, and $\chi_{\nu_{ul}}$ the dust opacity at the frequency ν_{ul} .

The observable line flux is obtained by integrating Eq. (10) in the vertical direction and summing up the integrals in the radial direction of the disk as,

$$F_{ul} = \frac{1}{4\pi d^2} \int_{x_{in}}^{x_{out}} 2\pi x dx \int_{-z_{\infty}}^{z_{\infty}} \tilde{\eta}_{ul}(x, z) dz, \quad (13)$$

where $\tilde{\eta}_{ul}(x, z)$ is the emissivity of the transition line at (x, z) times the effect of absorption in the upper disk layer,

$$\tilde{\eta}_{ul}(x, z) = n_u(x, z) A_{ul} \frac{h\nu_{ul}}{4\pi} \exp(-\tau_{ul}(x, z)), \quad (14)$$

and $\tau_{ul}(x, z)$ is the optical depth from z to the disk surface z_{∞} at the frequency ν_{ul} ,

$$\tau_{ul}(x, z) = \int_z^{z_{\infty}} \chi_{ul}(x, z') dz'. \quad (15)$$

Here, we use the distance to an object of $d = 56$ pc for calculating the intensity in order to compare it with the observations towards TW Hya.

4.1. The infrared spectra

The resulting line spectra in the near- and mid-infrared wavelength bands are plotted in Figs. 8a and 9a, respectively. The line spectra for the model without UV excess are presented in Figs. 8b and 9b for comparison. We can see from the figures that if the central star has a UV excess, the line spectra become stronger by about a few orders of magnitude because the strong UV irradiation by the central star heats the gas hot enough and makes the populations of the upper levels large, as we have seen in Sect. 3.2.

Some of the strongest line fluxes (F_{line}) we calculate for the models with (model A) and without (model B) UV excess radiation are listed in Table 1. The intensity ratios of the $2.12 \mu\text{m } v = 1 \rightarrow 0$ S(1) line to the $2.25 \mu\text{m } v = 2 \rightarrow 1$ S(1) line are ~ 80 and ~ 18 for model A and B, respectively. The corresponding excitation temperatures are ~ 900 K and ~ 1300 K, which are comparable to the kinetic temperature (cf. Fig. 2) as the level populations are in LTE (see Fig. 7). The excitation temperature is higher in the model without UV excess than in the model with UV excess because the emission comes mainly from the inner disk in the former case while it comes mostly from the outer cooler disk in the latter case as we will see below. The line ratio of the $2.12 \mu\text{m } v = 1 \rightarrow 0$ S(1) line to the $2.41 \mu\text{m } v = 1 \rightarrow 0$ Q(1), two of the strongest lines in Fig. 8, is larger for the model with UV excess for the same reason.

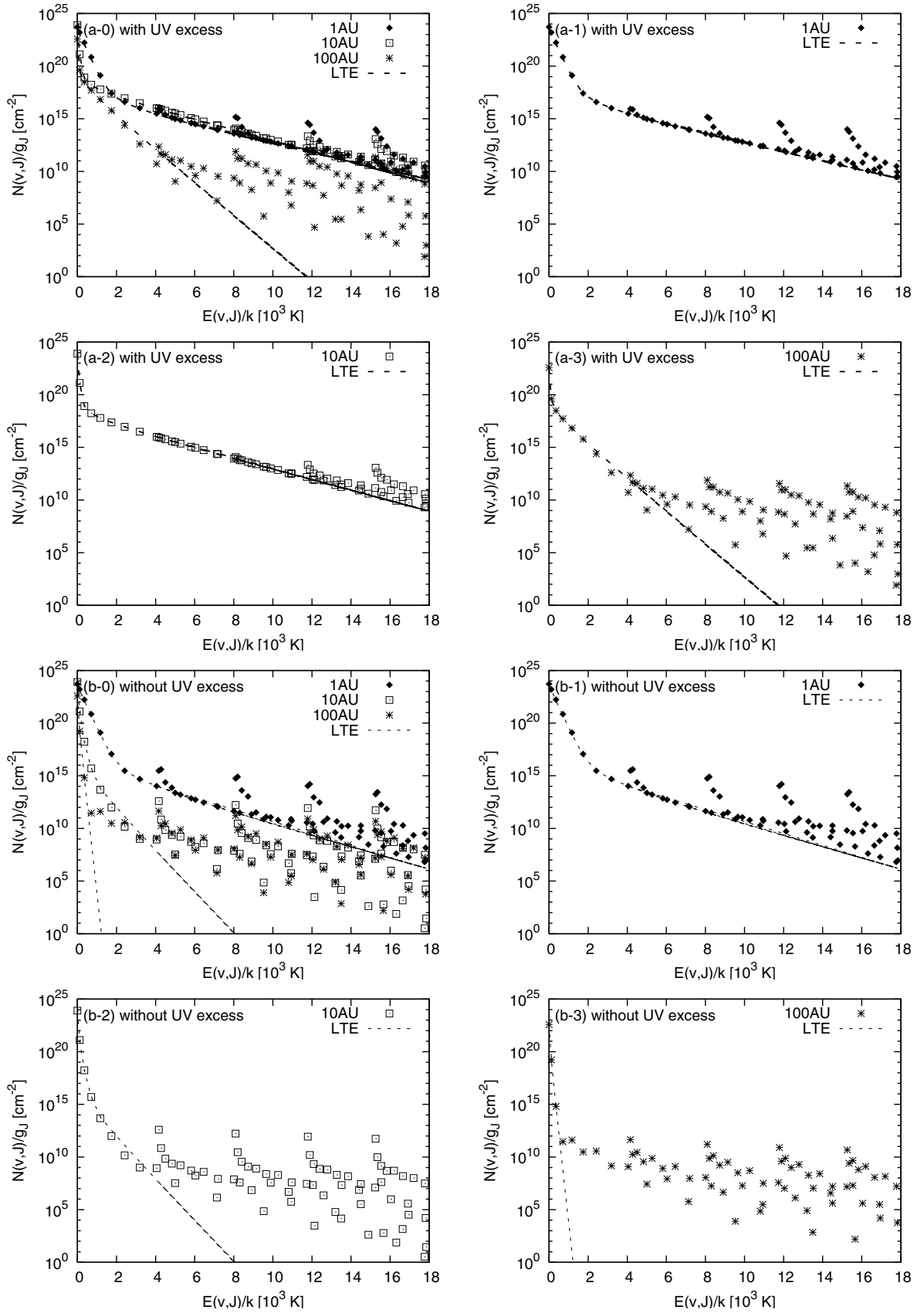


Fig. 7. The level populations of molecular hydrogen at the disk radii of $x = 1$ AU (filled diamonds), 10 AU (open squares) and 100 AU (asterisks) for the models **a**) with and **b**) without UV excess radiation. The LTE distributions are plotted in dashed lines. If the central star has a UV excess, the level populations are in LTE at the inner disk, and the populations of the upper levels become large due to the high temperature.

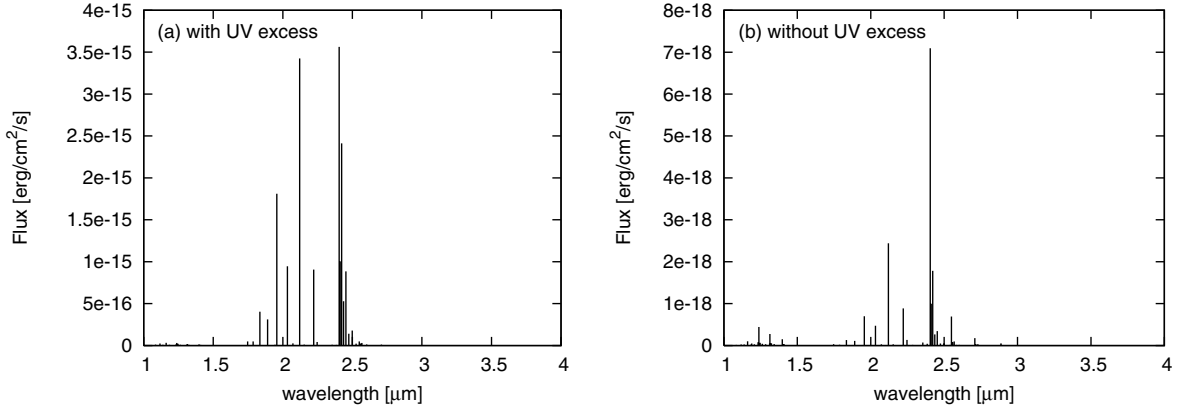


Fig. 8. The near-infrared ($1 \mu\text{m} < \lambda < 4 \mu\text{m}$) line spectra of molecular hydrogen from the disk in the model **a**) with and **b**) without UV excess radiation of the central star.

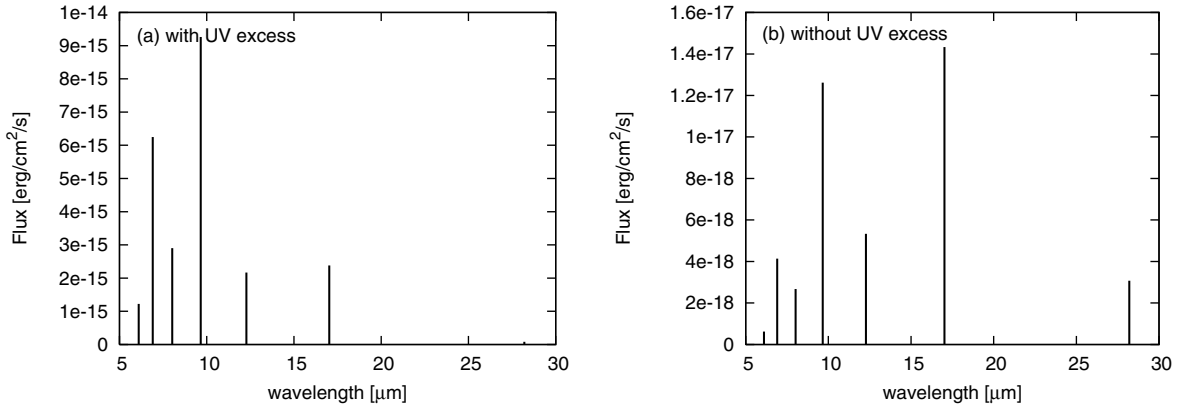


Fig. 9. Same as Fig. 8, but for the mid-infrared ($5 \mu\text{m} < \lambda < 30 \mu\text{m}$) wavelength band.

On the other hand, the pure rotational transition lines in Fig. 9 are emitted from all over the disk for both models since they trace the gas in cooler regions than the vib-rotational transition lines in Fig. 8 (see below). Therefore, the excitation temperature derived from the pure rotational transition lines for the model with UV excess is higher (that is, the weaker line flux for the lower level transitions) than that derived from the lines for the model without UV excess because the UV irradiation from the central star heats the gas in the disk more in the former model.

The observational intensity of the ro-vibrational line, $v = 1 \rightarrow 0$ S(1), towards TW Hya by Bary et al. (2003) is also presented in Table 1, and is comparable to our calculated flux in the model with UV excess. In addition, the observations of mid-infrared line spectra of pure rotational transitions, S(0) and S(1), by ISO (Thi et al. 2001b) and the upper limit of the line fluxes of S(1) and S(2) under the assumption of $FWHM$ of 30 km s^{-1} observed by TEXES at the NASA IRTF (Richter et al. 2002) are presented in Table 1. These are observed towards classical T Tauri stars in the Taurus-Auriga cloud complex ($d = 140 \text{ pc}$). We can see from the table that the calculated line fluxes are weaker than the results of the ISO observations, and consistent with the ground-based observations by TEXES. It may be that the spatial and wavelength resolutions of the ISO observations were not high enough so that the observed line emission comes not from the circumstellar disk

but from shocked regions in the associated outflows. The last two columns of Table 1 represent the flux of the calculated dust continuum emission from the disk plus the radiation from the central star ($F_{\text{cont.}}$) and the flux ratio of the molecular hydrogen line in model A to the continuum emission ($F_{\text{line}}/F_{\text{cont.}}$). The dust continuum emission is calculated by solving the radiative transfer equation (Eq. (10)), adopting $S_{ul} = B_{\nu_{ul}}(T_d)$ and $\chi_{ul} = \rho\chi_{\nu_{ul}}$ for the source term and the opacity, respectively. The central star is assumed to emit blackbody radiation with an effective temperature of $T_* = 4000 \text{ K}$ and a radius of $R_* = 2 R_{\odot}$.

Figure 10 represents the radial flux distributions, $dF_{ul}/dx = (2\pi x/4\pi d^2) \int_{-z_{\infty}}^{z_{\infty}} \tilde{\eta}_{ul} dz$, of the $2.12 \mu\text{m}$ $v = 1 \rightarrow 0$ S(1) line and the $28 \mu\text{m}$ S(0) line for the models with (solid line) and without (dashed line) UV excess radiation. The maximum gas temperature at each radius, $T_{\text{max}}(x) = \max\{T(x, z) | 0 < z < z_{\infty}\}$, is also plotted at the bottom of the figure. We can see from the figure that if the central star has a UV excess, the $2.12 \mu\text{m}$ $v = 1 \rightarrow 0$ S(1) line emission comes mainly from around the radius of 20 AU, which is consistent with that derived from the observed peak-to-peak velocity separation of the H_2 emission line due to the rotation velocity of the disk (Bary et al. 2003). The line flux distribution increases with increasing radius inside 20 AU since the line emissivity integrated over the vertical direction, $\int_{-z_{\infty}}^{z_{\infty}} \tilde{\eta}_{ul} dz$, does not change with radius and dF_{ul}/dx is almost proportional to the radius. This is because the transition

Table 1. The observed and calculated infrared line flux of molecular hydrogen (F_{line}), the calculated continuum radiation flux (F_{cont}) [erg/s/cm²], and the line-to-continuum flux ratio ($F_{\text{line}}/F_{\text{cont}}$).

λ (μm)	Line	F_{line}			F_{cont} ($\times 10^{-9}$)	$F_{\text{line}}^d/F_{\text{cont}}$ ($\times 10^{-6}$)
		Model A ($\times 10^{-15}$)	Model B ($\times 10^{-18}$)	Observation ($\times 10^{-15}$)		
1.16	2–0 S(1)	0.03	0.10		5.19	0.01
1.19	2–0 S(0)	0.01	0.05		5.09	0.00
1.24	2–0 Q(1)	0.03	0.44		4.91	0.01
1.24	2–0 Q(2)	0.01	0.05		4.90	0.00
1.25	2–0 Q(3)	0.02	0.06		4.87	0.00
1.83	1–0 S(5)	0.40	0.13		2.87	0.14
1.89	1–0 S(4)	0.31	0.11		2.73	0.11
1.96	1–0 S(3)	1.81	0.70		2.57	0.71
2.03	1–0 S(2)	0.95	0.47		2.40	0.39
2.12	1–0 S(1)	3.43	2.44	1.0 ^a	2.22	1.55
2.22	1–0 S(0)	0.91	0.89		2.03	0.45
2.25	2–1 S(1)	0.04	0.13		1.99	0.02
2.35	2–1 S(0)	0.01	0.07		1.81	0.01
2.41	1–0 Q(1)	3.56	7.09		1.74	2.05
2.41	1–0 Q(2)	1.00	1.00		1.73	0.58
2.42	1–0 Q(3)	2.41	1.78		1.71	1.41
2.44	1–0 Q(4)	0.53	0.27		1.69	0.31
2.45	1–0 Q(5)	0.88	0.34		1.67	0.53
2.47	1–0 Q(6)	0.14	0.05		1.64	0.09
2.50	1–0 Q(7)	0.18	0.06		1.61	0.11
2.55	2–1 Q(1)	0.05	0.69		1.55	0.03
2.56	2–1 Q(2)	0.01	0.08		1.54	0.01
2.57	2–1 Q(3)	0.03	0.10		1.52	0.02
6.11	0–0 S(6)	1.22	0.62		0.25	4.98
6.91	0–0 S(5)	6.25	4.14		0.19	32.06
8.02	0–0 S(4)	2.90	2.67		0.18	16.10
9.66	0–0 S(3)	9.26	12.62		0.24	38.37
12.27	0–0 S(2)	2.17	5.33	<30 ^c	0.15	14.28
17.02	0–0 S(1)	2.38	14.33	28–81 ^b , <39 ^c	0.13	18.62
28.20	0–0 S(0)	0.08	3.08	25–57 ^b	0.09	0.94

^a Observation by Bary et al. (2003).^b Observations by Thi et al. (2001b).^c Observations by Richter et al. (2002).^d F_{line} in model A.

line arises from hot gas with $T > 1000$ K and the maximum gas temperature of the disk satisfies this condition. The maximum temperature does not change very much at $x < 20$ AU due to the weak dependence of the photoelectric heating rate on the UV photon flux in this range (see e.g., Weingartner & Draine 2001b). Meanwhile, the line flux distribution decreases suddenly beyond 20 AU because the gas temperature falls rapidly below 1000 K due to the stronger dependence of the photoelectric heating rate on the UV flux in this range. For the model without UV excess, the line emission mainly

comes from the very inner region of the disk, $x < 0.3$ AU, because the UV irradiation by the central star is not strong enough to heat the gas at the outer disk to high enough temperatures as we have seen in Sect. 2.4. The line flux distribution increases with increasing radius at the outer disk, $x > 3$ AU, since the populations of the ro-vibrational levels are controlled not by the collisional excitation but by the UV pumping process (see Fig. 7b), and the radiation energy density integrated over the vertical direction is almost constant to the radius in this region.

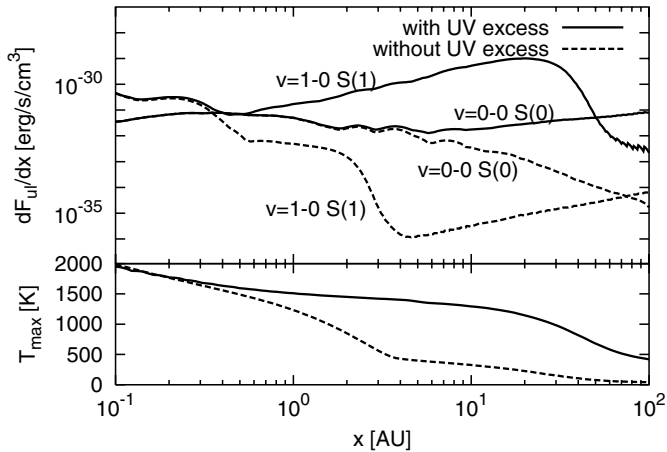


Fig. 10. The radial flux distributions of the $2.12 \mu\text{m } v = 1-0 \text{ S}(1)$ line and the $28 \mu\text{m S}(0)$ line for the models with (solid line) and without (dashed line) UV excess radiation (*top*). The maximum gas temperature at each radius is also plotted at the bottom. If the central star has UV excess radiation, the $2.12 \mu\text{m } v = 1-0 \text{ S}(1)$ line emission comes mainly from the radius of 20 AU, while the $28 \mu\text{m S}(0)$ line emission comes from all over the disk.

The $28 \mu\text{m S}(0)$ line emission comes from a cooler region, compared with the $2.12 \mu\text{m } v = 1 \rightarrow 0 \text{ S}(1)$ line, with the gas temperature of $T > 100 \text{ K}$. If the central star has UV excess radiation, the radial flux distribution of the line is almost constant all over the disk, that is, the line emissivity integrated over the vertical direction decreases with increasing radius. This is because the gas is heated up to $T > 100 \text{ K}$ even in the dense region near the midplane in the inner disk, while it is heated up only in the less dense region of the disk surface in the outer disk (see Fig. 2a). Meanwhile, for the model without UV excess, the gas temperature does not reach 100 K at $x > 20 \text{ AU}$ (see Fig. 2b), which makes the line flux very weak at the outer disk. The flux distributions for the models with and without UV excess are identical at the inner disk, $x < 3 \text{ AU}$, because the gas temperature reaches 100 K even in the region where it is controlled by the dust temperature through gas–grain collisions, and the dust temperatures are identical in both models (see Fig. 2).

Furthermore, the vertical profiles of the emissivity, $\tilde{\eta}_{ul}$ (Eq. (14)), of the $2.12 \mu\text{m } v = 1 \rightarrow 0 \text{ S}(1)$ line and the $28 \mu\text{m S}(0)$ line at 10 AU for the models with (solid line) and without (dashed line) UV excess radiation are plotted in Fig. 11. We can see from the figure that in the surface layer of the disk the emissivity of both lines for both models basically increases with decreasing vertical height due to the increasing gas density. For the model with UV excess radiation, the emissivity of the $2.12 \mu\text{m } v = 1 \rightarrow 0 \text{ S}(1)$ line decreases suddenly where the gas temperature falls below $\sim 1000 \text{ K}$. The corresponding disk height is $z \sim 3.5 \text{ AU} \sim 17H$, where $H = c_s/\Omega$ is the disk scale height. The optical depth from the disk surface to $z \sim 3.5 \text{ AU}$ is small enough, $\tau_{ul} \sim 1.5 \times 10^{-3}$, for the line. Meanwhile, in the model without UV excess, it is independent of the gas temperature because the level populations are controlled by the UV pumping process (see Sect. 3.2), and it decreases near the midplane where the UV irradiation

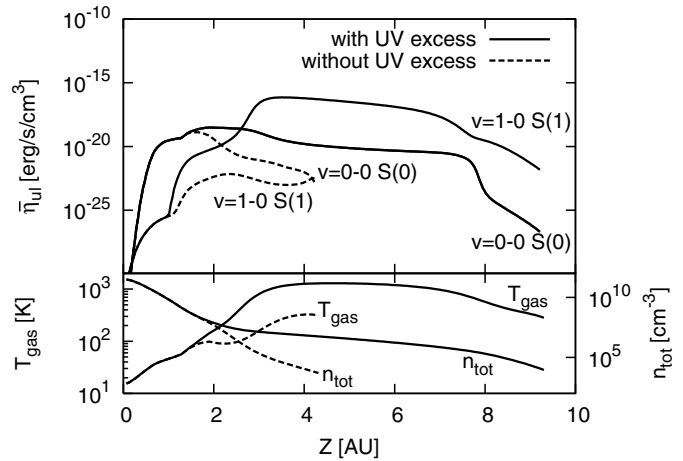


Fig. 11. The vertical profiles of the emissivity of the $2.12 \mu\text{m } v = 1-0 \text{ S}(1)$ line and the $28 \mu\text{m S}(0)$ line at the radius of 10 AU for the models with (solid line) and without (dashed line) UV excess radiation (*top*). The vertical profiles of the gas temperature and density are also plotted at the bottom. For the model with UV excess radiation, the $2.12 \mu\text{m } v = 1-0 \text{ S}(1)$ line emission comes from hot surface layer with $T_{\text{gas}} > 1000 \text{ K}$, while the $28 \mu\text{m S}(0)$ line emission comes from cooler region near the midplane with $T_{\text{gas}} > 50 \text{ K}$.

cannot penetrate. The emissivity of the $28 \mu\text{m S}(0)$ line has a peak where the gas temperature drops below 100 K in both models. The corresponding disk height is $z \sim 1.9 \text{ AU} \sim 9.5H$, where the line is also optically thin ($\tau_{ul} \sim 6.6 \times 10^{-3}$) for the model with UV excess. The emissivity in the far cooler region close to the midplane is still relatively large due to the high gas density, but it decreases distinctly at $T < 50 \text{ K}$. Therefore, although the gas in the disk is concentrated near the midplane, these lines come only from the upper region of the disk. Also, the figure indicates that the line flux traces the gas density and temperature where the gas temperature falls below the critical value.

4.2. The ultraviolet spectra

The resulting line spectra in the ultraviolet wavelength band are plotted in Figs. 12a and 12b for the models with and without UV excess radiation, respectively. If the central star has a UV excess, some of those lines, whose upper levels are in excited electronic states and populated via the UV pumping process, become stronger by more than six orders of magnitude than those in the model without UV excess.

Some of the strongest line fluxes we calculate in the model with UV excess (model A) are listed in Table 2 and compared with observations by the HST and the FUSE (Herczeg et al. 2002). The calculated strong line fluxes result from the excitation due to the strong Ly α line emission from the central star and are consistent with the observations. The line fluxes in the model without UV excess (model B) are also presented in the table for comparison. In addition, in order to see the effect of pumping by Ly α emission, we calculate the level populations and UV line fluxes by neglecting Ly α emission (model C). The gas density and temperature profiles for the model with UV excess are used here. The resulting line emission is presented

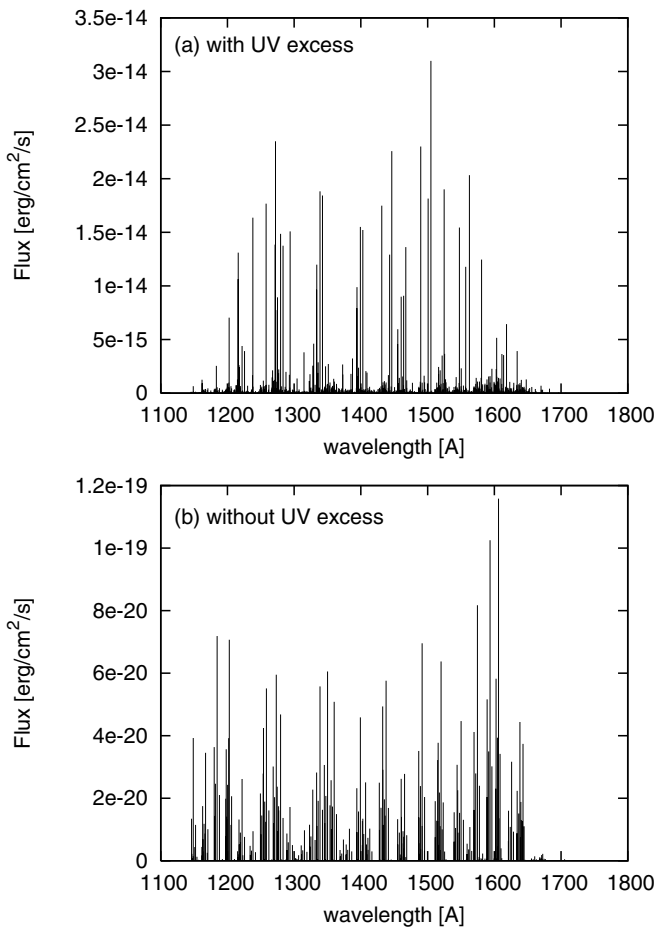


Fig. 12. Same as Fig. 8, but for the ultraviolet ($1100 \text{ \AA} < \lambda < 1800 \text{ \AA}$) wavelength band.

in Fig. 13 and Table 2, and is much weaker than the observed values.

The level populations in the excited electronic state at the radius of 10 AU and the vertical height of 6 AU for models A (asterisks) and C (open squares) are plotted in Fig. 14. Figures labeled (1) and (2) show the level populations for models A and C, respectively, and they are plotted together in figure (0) for comparison. The dotted lines in figure (0) connect the level populations of models A and C in the same energy levels. The figures clearly show that specific level populations are extremely high for model A (with UV excess radiation) due to the irradiation of the Ly α emission from the central star. The transitions from these levels result in the strong line emission in Fig. 12a. Meanwhile, the level populations for model C (without Ly α emission) are low and distributed smoothly since they are excited only by continuum radiation. This is why the line fluxes are weak and many lines have similar strength in Fig. 13.

In the case of model B (without UV excess) the line spectra are much weaker (Fig. 12b) due to the weak UV irradiation from the central star and the low level populations of pre-excited hydrogen molecules in the ground electronic state (Fig. 7b, see also below). Also, the line spectra are relatively scattered, although they result from the pumping by continuum irradiation. This is because molecular hydrogen in highly

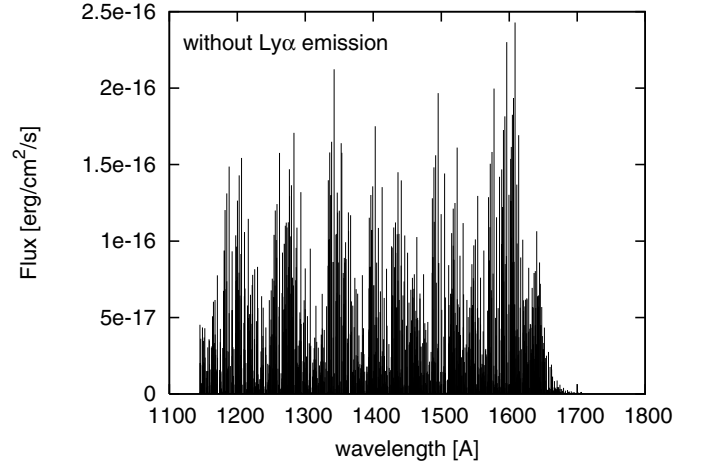


Fig. 13. The ultraviolet line spectra of molecular hydrogen for the model without Ly α line emission from the central star.

excited electronic states originates mainly from highly populated low energy levels ($v = 0$) in the ground electronic state, whose populations decrease suddenly with increasing level energies due to the low temperature for the model without UV excess (Fig. 7b). Thus, the level populations in the excited electronic state also have steeper distributions, which lead to the sparse line spectra.

Figure 15 shows the radial flux distribution of the 1272.0 \AA $v = 1 \rightarrow 3$ P(5) line, which is one of the strongest lines in model A, for the models with (solid line) and without (dashed line) UV excess radiation, and without Ly α emission (dotted line). The flux decreases with increasing radius for all models because the line intensity is proportional to the population of the upper transition level in the excited electronic state, namely, the UV irradiation flux from the central star which is proportional to the inverse squares of the radius at the disk surface.

The vertical profiles of the line emissivity at 10 AU for these models are also plotted in Fig. 16 (top). At the disk surface, the profiles of $\tilde{\eta}_{ul}$ are similar to those of the number densities of pre-excited hydrogen molecules in the ground electronic state, $n(v, J)$, plotted in the bottom of Fig. 16. This is because the line emissivity is proportional to the number density of H $_2$ in the upper transition level of the line, $n(v^* = 1, J^* = 4)$ (the symbol * means that it is in the excited electronic state), which is populated via the UV pumping process and proportional to both $n(v, J)$ and the UV irradiation flux, $F_{\nu(vJ \rightarrow v^*J^*),R} + F_{\nu(vJ \rightarrow v^*J^*),z}$ (Eqs. (6) and (7)). In the models without UV excess and without Ly α emission, the level ($v^* = 1, J^* = 4$) is populated mainly from the highly populated low energy level, ($v = 0, J = 3$). Meanwhile, in the model with UV excess, the transition from the level ($v = 2, J = 5$) dominates in populating the level ($v^* = 1, J^* = 4$) because the excitation wavelength, $\lambda = hc/E(v = 2, J = 5 \rightarrow v^* = 1, J^* = 4) = 1216.2 \text{ \AA}$, is close to the central wavelength of the Ly α line emission. So, the number density of $n(v = 0, J = 3)$ is plotted for the models without UV excess and without Ly α emission, while that of $n(v = 2, J = 5)$ is plotted for the model with UV excess in the

Table 2. The observed and calculated ultraviolet line flux of molecular hydrogen [erg/s/cm²].

λ (Å)	Line	Model A ($\times 10^{-15}$)	Model B ($\times 10^{-21}$)	Model C ($\times 10^{-16}$)	Obs. ^a ($\times 10^{-15}$)	λ (Å)	Line	Model A ($\times 10^{-15}$)	Model B ($\times 10^{-21}$)	Model C ($\times 10^{-16}$)	Obs. ^a ($\times 10^{-15}$)
1161.7	0–1 R(0)	0.16	4.42	0.08		1148.7	1–1 R(3)	0.65	0.04	0.18	4.6
1166.3	0–1 P(2)	0.25	8.74	0.14		1161.9	1–1 P(5)	1.25	0.05	0.30	10.9
1217.3	0–2 R(0)	2.61	13.22	0.37		1202.5	1–2 R(3)	7.04	0.08	0.79	11.3
1222.0	0–2 P(2)	4.40	26.14	0.71		1216.2	1–2 P(5)	13.11	0.09	1.15	
1274.6	0–3 R(0)	7.75	23.68	0.70	27.4	1257.9	1–3 R(3)	17.68	0.06	0.89	18.1
1279.6	0–3 P(2)	14.86	46.82	1.37	39.2	1272.0	1–3 P(5)	23.49	0.07	1.12	20.5
1333.6	0–4 R(0)	9.64	28.21	0.84	42.8	1314.8	1–4 R(3)	3.81	0.01	0.17	12.2
1338.7	0–4 P(2)	18.83	55.75	1.65	73.1	1329.3	1–4 P(5)	4.61	0.01	0.21	7.5
1393.9	0–5 R(0)	7.94	23.21	0.69	35.3	1372.7	1–5 R(3)	2.67	0.01	0.12	3.2
1399.1	0–5 P(2)	15.51	45.88	1.36	73.8	1387.5	1–5 P(5)	3.23	0.01	0.15	7.1
1455.0	0–6 R(0)	4.59	13.28	0.40	20.8	1431.2	1–6 R(3)	17.48	0.06	0.83	29.0
1460.4	0–6 P(2)	9.00	26.23	0.78	41.6	1446.3	1–6 P(5)	22.57	0.07	1.04	44.2
1516.4	0–7 R(0)	1.78	5.08	0.15	21.2	1489.8	1–7 R(3)	23.00	0.08	1.13	48.2
1521.8	0–7 P(2)	3.50	10.03	0.30	16.2	1505.0	1–7 P(5)	30.99	0.09	1.44	57.5
1577.3	0–8 R(0)	0.42	1.18	0.04		1547.6	1–8 R(3)	15.45	0.05	0.74	35.3
1582.6	0–8 P(2)	0.83	2.33	0.07		1562.7	1–8 P(5)	20.33	0.06	0.94	37.2
1636.4	0–9 R(0)	0.05	0.13	0.00		1603.5	1–9 R(3)	5.16	0.02	0.24	11.2
1641.7	0–9 P(2)	0.09	0.26	0.01		1618.2	1–9 P(5)	6.44	0.02	0.29	11.6
1692.5	0–10 R(0)	0.00	0.00	0.00		1656.2	1–10 R(3)	0.57	0.00	0.03	
1697.6	0–10 P(2)	0.00	0.01	0.00		1670.0	1–10 P(5)	0.69	0.00	0.03	
1162.2	0–1 R(1)	0.17	1.74	0.09		1162.0	1–1 R(6)	0.91	0.00	0.14	
1169.8	0–1 P(3)	0.28	2.55	0.15		1183.4	1–1 P(8)	2.55	0.00	0.24	
1217.7	0–2 R(1)	2.43	5.21	0.52	9.1	1215.8	1–2 R(6)	10.64	0.00	0.49	
1225.6	0–2 P(3)	3.93	7.64	0.82		1238.0	1–2 P(8)	16.37	0.01	0.56	11.5
1275.0	0–3 R(1)	8.94	9.33	1.12	24.6	1271.2	1–3 R(6)	13.84	0.00	0.43	14.1
1283.2	0–3 P(3)	13.74	13.70	1.71	28.0	1294.0	1–3 P(8)	15.09	0.00	0.46	13.0
1333.9	0–4 R(1)	11.98	11.12	1.40	7.9	1327.8	1–4 R(6)	2.55	0.00	0.08	6.1
1342.4	0–4 P(3)	18.43	16.32	2.12	64.9	1351.2	1–4 P(8)	2.72	0.00	0.08	2.8
1394.1	0–5 R(1)	9.89	9.15	1.15	52.4	1385.2	1–5 R(6)	1.79	0.00	0.05	
1402.8	0–5 P(3)	15.21	13.44	1.75	73.1	1409.2	1–5 P(8)	1.91	0.00	0.06	2.2
1455.2	0–6 R(1)	5.97	5.24	0.68	30.9	1443.1	1–6 R(6)	12.92	0.00	0.39	11.3
1464.0	0–6 P(3)	9.08	7.68	1.03	42.1	1467.4	1–6 P(8)	13.62	0.00	0.42	17.6
1516.5	0–7 R(1)	2.45	2.00	0.27	21.2	1500.7	1–7 R(6)	18.14	0.00	0.55	19.7
1525.4	0–7 P(3)	3.66	2.94	0.41	17.9	1524.9	1–7 P(8)	19.01	0.01	0.59	23.5
1577.1	0–8 R(1)	0.60	0.47	0.07		1557.2	1–8 R(6)	11.78	0.00	0.36	17.0
1586.0	0–8 P(3)	0.88	0.68	0.10		1581.0	1–8 P(8)	12.46	0.00	0.38	17.5
1636.1	0–9 R(1)	0.07	0.05	0.01		1611.3	1–9 R(6)	3.65	0.00	0.11	
1644.8	0–9 P(3)	0.10	0.08	0.01		1634.2	1–9 P(8)	3.92	0.00	0.12	5.5
1692.0	0–10 R(1)	0.00	0.00	0.00		1661.5	1–10 R(6)	0.39	0.00	0.01	
1700.3	0–10 P(3)	0.00	0.00	0.00		1682.8	1–10 P(8)	0.42	0.00	0.01	

^a Observations by Herczeg et al. (2002).

bottom of Fig. 16. The line emissivity decreases with decreasing vertical height for all models especially near the midplane because the irradiating UV photons are self-absorbed (used for

the pumping) and can not penetrate deep in the disk. Thus, the molecular hydrogen emission from near the midplane is not observable in the ultraviolet region.

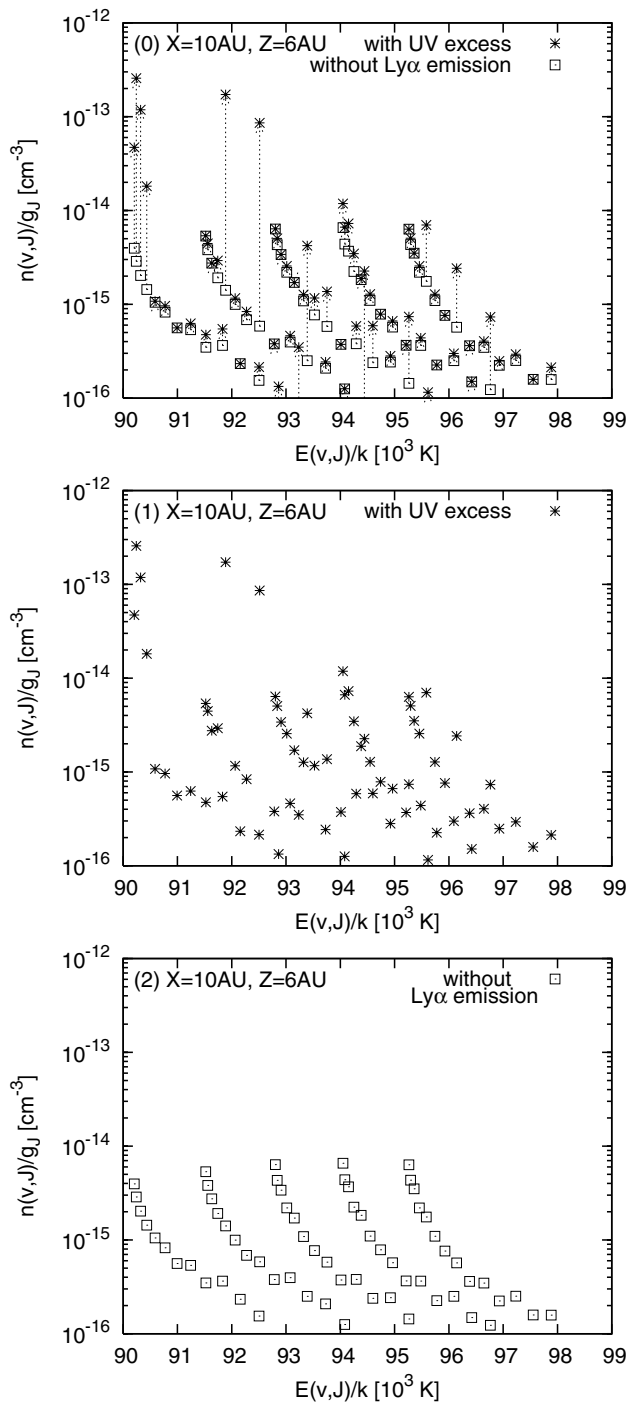


Fig. 14. The level populations in the excited electronic state at $(X, Z) = (10 \text{ AU}, 6 \text{ AU})$ for the models with UV excess (asterisks) and without $\text{Ly}\alpha$ emission (open squares). Some specific levels are highly populated due to irradiation by the strong $\text{Ly}\alpha$ line emission from the central star.

5. Summary

We have, for the first time, investigated molecular hydrogen emission from protoplanetary disks, taking into account the global physical structure of the disk and the detailed analysis of level populations of molecular hydrogen.

First, we obtained in a self-consistent manner the density and temperature profiles of gas and dust, taking into account

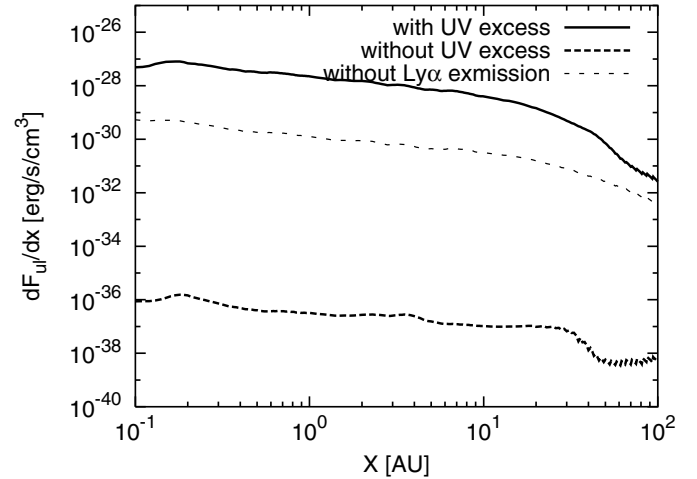


Fig. 15. The radial flux distributions of the $1272.0 \text{ \AA } v = 1 \rightarrow 3 \text{ P}(5)$ line for the models with (solid line) and without (dashed line) UV excess radiation, and without $\text{Ly}\alpha$ emission (dotted line). The radiation flux decreases with increasing radius for all models because the UV irradiation flux, which pumps hydrogen molecules in the ground electronic state, decreases.

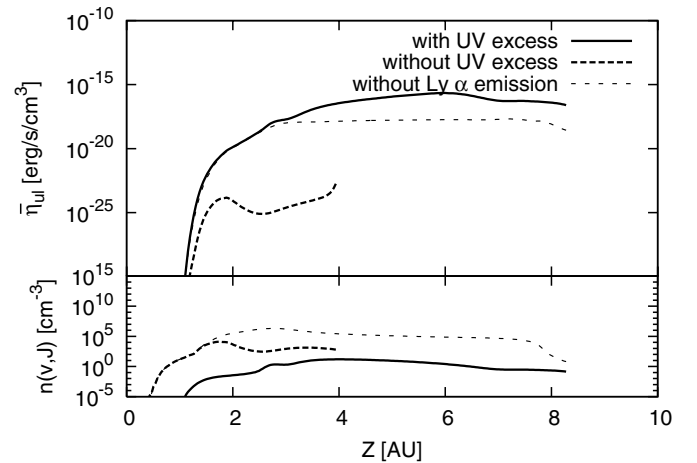


Fig. 16. The vertical profiles of the emissivity of the $1272.0 \text{ \AA } v = 1 \rightarrow 3 \text{ P}(5)$ line at the radius of 10 AU for the models with (solid line) and without (dashed line) UV excess radiation, and without $\text{Ly}\alpha$ emission (dotted line) (*top*). The energy density profiles are similar to the number density profiles of H_2 in the pre-excited level in the ground electronic state (*bottom*).

the irradiation by a central T Tauri star. As a result, we found that if the central star has UV excess emission over the photospheric blackbody radiation, the gas temperature at the disk surface can reach about 1000 K even at the radius of 10 AU due to grain photoelectric heating induced by the UV photons from the central star.

Next, making use of the physical structure of the disk, we calculated the level populations of molecular hydrogen in its ground electronic state on the assumption of statistical equilibrium. The resulting level populations tend to be in LTE, although the populations in the upper levels become very large due to the high gas temperature if the central star has UV excess radiation.

Furthermore, using these level populations, we computed molecular hydrogen emission in the near- and mid-infrared and ultraviolet wavelength bands by solving the radiative transfer equation. Consequently, we found strong line emission spectra if the central star has UV excess radiation. The infrared line spectra are strong because the populations of the upper levels become large due to the high gas temperature, while the ultraviolet line emission is intense because the strong UV irradiation, including that due to Ly α , by the central star pumps the hydrogen molecule from the ground to the excited electronic states. We compared the results of our calculation with the observations to find that the calculated near-infrared intensity of the $v = 1 \rightarrow 0$ S(1) line is in good agreement with that observed towards TW Hya, as are the ultraviolet lines. Our predictions for the pure rotational line intensities are much below those observed by Thi et al. (2001b) but this may be related to the large ISO beam used.

Acknowledgements. We would like to thank an anonymous referee for his/her comments which improved our paper. We are also grateful to Dr. R. Wagenblast for giving us the numerical code for molecular hydrogen level populations. Astrophysics at UMIST and the University of Manchester is supported by a grant from PPARC. Also, H.N. is supported by “The 21st Century COE Program of Origin and Evolution of Planetary Systems” in MEXT and the Research Fellowships of the JSPS 16036205 and 15540237.

References

- Adams, F. C., & Shu, F. H. 1986, *ApJ*, 308, 836
Aikawa, Y., van Zadelhoff, G. J., van Dishoeck, E. F., & Herbst, E. 2002, *A&A*, 386, 622
Anders, E., & Grevesse, N. 1989, *Geochim. Cosmochim. Acta*, 53, 197
Ardila, D. R., Basri, G., Walter, F. M., Valenti, J. A., & Johns-Krull, C. M. 2002, *ApJ*, 566, 1100
Bary, J. S., Weintraub, D. A., & Kastner, J. H. 2002, *ApJ*, 576, L73
Bary, J. S., Weintraub, D. A., & Kastner, J. H. 2003, *ApJ*, 586, 1136
Beckwith, S., Gatley, I., & Persson, S. E. 1978, *ApJ*, 219, L33
Beckwith, S. V. W., & Sargent, A. I. 1993, in *Protostars and Planets III*, ed. E. H. Levy, & J. Lunine (Tucson, Univ. Arizona Press), 521
Bergin, E. A., Calvet, N., D’Alessio, P., & Herczeg, G. J. 2003, *ApJ*, 591, L159
Bergin, E., Calvet, N., Sitko, M. L., et al. 2004, *ApJ*, 614, L133
Black, J. H., & Dalgarno, A. 1976, *ApJ*, 203, 132
Black, J. H., & Dalgarno, A. 1977, *ApJS*, 34, 405
Black, J. H., & van Dishoeck, E. F. 1987, *ApJ*, 322, 412
Bohren, C. F., & Huffman, D. R. 1983, *Absorption and scattering of light by small particles* (New York: Wiley)
Brown, A., Millar, T. J., Williams, P. M., & Zealey, W. J. 1983, *MNRAS*, 203, 785
Burke, J. R., & Hollenbach, D. J. 1983, *ApJ*, 265, 223
Burrows, C. J., Stapelfeldt, K. R., Watson, A. M., et al. 1996, *ApJ*, 473, 437
Burton, M. G., Bulmer, M., Moorhouse, A., Gaballe, T. R., & Brand, P. W. J. L. 1992, *MNRAS*, 257, 1
Calvet, N., & Gullbring, E. 1998, *ApJ*, 509, 802
Cardelli, J. A., Clayton, G. C., & Mathis, J. S. 1989, *ApJ*, 345, 245
Cazaux, S., & Tielens, A. G. G. M. 2002, *ApJ*, 575, L29
Cazaux, S., & Tielens, A. G. G. M. 2004, *ApJ*, 604, 222
Chiang, E. I., & Goldreich, P. 1997, *ApJ*, 490, 368
Cohen, M. 1974, *MNRAS*, 169, 257
Costa, V. M., Lago, M. T. V. T., Norci, L., & Meurs, E. J. A. 2000, *A&A*, 354, 621
Cotera, A. S., Whitney, B. A., Young, E., et al. 2001, *ApJ*, 556, 958
D’Alessio, P., Cantó, J., Calvet, N., & Lizano, S. 1998, 500, 411
de Jong, T., Dalgarno, A., & Boland, W. 1980, *A&A*, 91, 68
Draine, B., & Lee, H. M. 1984, *ApJ*, 285, 89
Draine, B. T. 1978, *ApJS*, 36, 595
Draine, B. T., & Bertoldi, F. 1996, *ApJ*, 468, 269
Draine, B. T., Roberge, W. G., & Dalgarno, A. 1983, *ApJ*, 264, 485
Duley, W. W., & Williams, D. A. 1986, *MNRAS*, 223, 177
Dullemond, C. P., & Dominik, C. 2004, *A&A*, 421, 1075
Dullemond, C. P., & Natta, A. 2003, *A&A*, 408, 161
Dullemond, C. P., & Turolla, R. 2000, *A&A*, 360, 1187
Dullemond, C. P., van Zadelhoff, G. J., & Natta, A. 2002, *A&A*, 389, 464
Dutrey, A., Guilloteau, S., & Guelin, M. 1997, *A&A*, 317, L55
Federman, S. R., Glassgold, A. E., & Kwan, J. 1979, *ApJ*, 227, 466
Fukagawa, M., Hayashi, M., Tamura, M., et al. 2004, *ApJ*, 605, L53
Glassgold, A. E., Najita, J., & Igea, J. 2004, *ApJ*, 615, 972
Gorti, U., & Hollenbach, D. 2004, *ApJ*, 613, 424
Habing, H. J. 1968, *Bull. Astron. Inst. Netherlands*, 19, 421
Hasegawa, T., Gatley, I., Garden, R. P., et al. 1987, *ApJ*, 318, L77
Herbig, G. H., & Goodrich, R. W. 1986, *ApJ*, 309, 294
Herbst, W., Herbst, D. K., Grossman, E. J., & Weinstein, D. 1994, *AJ*, 108, 1906
Herczeg, G. J., Linsky, J. L., Valenti, J. A., Johns-Krull, C. M., & Wood, B. E. 2002, *ApJ*, 572, 310
Herczeg, G. J., Wood, B. E., Linsky, J. L., Valenti, J. A., & Johns-Krull, C. M. 2004, *ApJ*, 607, 369
Hollenbach, D., Johnstone, D., Lizano, S., & Shu, F. 1994, *ApJ*, 428, 654
Hollenbach, D., & McKee, C. F. 1979, *ApJS*, 41, 555
Itoh, Y., Sugitani, K., Ogura, K., & Tamura, M. 2003, *PASJ*, 55, L77
Jayawardhana, R., Luhman, K. L., D’Alessio, P., & Stauffer, J. R. 2002, *ApJ*, 571, L51
Johns-Krull, C. M., Valenti, J. A., & Linsky, J. L. 2000, *ApJ*, 539, 815
Jonkheid, B., Faas, F. G. A., van Zadelhoff, G.-J., & van Dishoeck, E. F. 2004
Kamp, I., & Dullemond, C. P. 2004, *ApJ*, 615, 991
Kamp, I., & van Zadelhoff, G.-J. 2001, *A&A*, 373, 641
Kenyon, S. J., & Hartmann, L. 1987, *ApJ*, 323, 714
Kenyon, S. J., & Hartmann, L. 1995, *ApJS*, 101, 117
Kusaka, T., Nakano, T., & Hayashi, C. 1970, *Prog. Theor. Phys.*, 44, 1580
Lago, M. T. V. T., Penston, M. V., & Johnstone, R. 1984, in *Proc. of the Fourth European IUE Conference*, ed. E. J. Rolfe, & B. Battrick, ESA SP-218, 233
Langer, W. D. 1976, *ApJ*, 206, 699
Laor, A., & Draine, B. T. 1993, *ApJ*, 402, 441
Lepp, S., Buch, V., & Dalgarno, A. 1995, *ApJS*, 98, 345
Le Teuff, Y. H., Millar, T. J., & Markwick, A. J. 2000, *A&AS*, 146, 157
Li, A., & Draine, B. T. 2001, *ApJ*, 554, 778
Lynden-Bell, D., & Pringle, J. E. 1974, *MNRAS*, 168, 603
Markwick, A. J., Ilgner, M., Millar, T. J., & Henning, T. 2002, *A&A*, 385, 632
Mathis, J. S., Rimpl, W., & Nordsieck, K. H. 1977, *ApJ*, 217, 425
Miyake, K., & Nakagawa, Y. 1993, *Icarus*, 106, 20
Nelson, R. P., & Langer, W. D. 1997, *ApJ*, 482, 796
Nomura, H. 2002, *ApJ*, 567, 587
Osterbrock, D. E. 1989, *Astrophysics of Gaseous Nebulae and Active Galactic Nuclei* (University Science Books)
Ostriker, E. C., & Shu, F. H. 1995, *ApJ*, 447, 813

- Padgett, D. L., Brandner, W., Stapelfeldt, K. R., et al. 1999, *AJ*, 117, 1490
- Pineau des Forets, G., Flower, D. R., Hartquist, T. W., & Dalgarno, A. 1986, *MNRAS*, 220, 801
- Pirronello, V., Liu, C., Roser, J. E., & Vidali, G. 1999, *A&A*, 344, 681
- Pringle, J. E. 1981, *ARA&A*, 19, 137
- Richter, M. J., Jaffe, D. T., Blake, G. A., & Lacy, J. H. 2002, *ApJ*, 572, L161
- Rybicki, G. B., & Lightman, A. P. 1979, *Radiative Processes in Astrophysics* (San Francisco)
- Sako, S., Yamashita, T., Kataza, H., et al. 2005, *ApJ*, 620, 347
- Sheret, I., Ramsay Howat, S. K., & Dent, W. R. F. 2003, *MNRAS*, 343, L65
- Shull, J. M. 1978, *ApJ*, 219, 877
- Smith, D., Adams, N. G., & Alge, E. 1982, *ApJ*, 263, 123
- Stapelfeldt, K. R., Krist, J. E., Ménard, F., et al. 1998, *ApJ*, 502, L65
- Stapelfeldt, K. R., Ménard, F., Watson, A. M., et al. 2003, *ApJ*, 589, 410
- Sternberg, A. 1988, *ApJ*, 332, 400
- Sternberg, A. 1989, *ApJ*, 347, 863
- Sternberg, A., & Dalgarno, A. 1989, *ApJ*, 338, 197
- Storzer, H., & Hollenbach, D. 1998, *ApJ*, 502, L71
- Takahashi, J., & Uehara, H. 2001, *ApJ*, 561, 843
- Thi, W., van Dishoeck, E. F., Blake, G. A., van Zadelhoff, G., & Hogerheijde, M. R. 1999, *ApJ*, 521, L63
- Thi, W. F., Blake, G. A., van Dishoeck, E. F., et al. 2001a, *Nature*, 409, 60
- Thi, W. F., van Dishoeck, E. F., Blake, G. A., et al. 2001b, *ApJ*, 561, 1074
- Tielens, A. G. G. M., & Hollenbach, D. 1985, *ApJ*, 291, 722
- Tiné, S., Lepp, S., Gredel, R., & Dalgarno, A. 1997, *ApJ*, 481, 282
- Valenti, J. A., Johns-Krull, C. M., & Linsky, J. L. 2000, *ApJS*, 129, 399
- van Dishoeck, E. F., & Black, J. H. 1982, *ApJ*, 258, 533
- van Zadelhoff, G. J., Aikawa, Y., Hogerheijde, M. R., & van Dishoeck, E. F. 2003, *A&A*, 397, 789
- Wagenblast, R., & Hartquist, T. W. 1988, *MNRAS*, 230, 363
- Weingartner, J. C., & Draine, B. T. 2001a, *ApJ*, 548, 296 (WD01a)
- Weingartner, J. C., & Draine, B. T. 2001b, *ApJS*, 134, 263
- Weintraub, D. A., Kastner, J. H., & Bary, J. S. 2000, *ApJ*, 541, 767
- Zecho, T., Gürtler, A., Sha, X., Jackson, B., & Küppers, J. 2002, *J. Chem. Phys.*, 117, 8486

Online Material

Appendix A: Thermal processes

The following three processes which are dominant under conditions in protoplanetary disks are considered as heating and cooling processes in this paper.

A.1. Grain photoelectric heating

The photoelectric emission from dust grains induced by far ultraviolet (FUV) photons from the central star dominates the heating at the surface layer of protoplanetary disks (see Sect. 2.4), especially if the star has UV excess radiation (Sect. 2.2 and Appendix C). In this paper we adopt the photoelectric heating rate calculated by Weingartner & Draine (2001b),

$$\Gamma_{\text{pe}} = 1.0 \times 10^{-26} \epsilon G_{\text{FUV}} n_{\text{tot}} \text{ erg cm}^{-3} \text{ s}^{-1}, \quad (\text{A.1})$$

$$\epsilon = \frac{C_0 + C_1 T^4}{1 + C_2 (G_{\text{FUV}} \sqrt{T}/n_e)^{C_5} [1 + C_3 (G_{\text{FUV}} \sqrt{T}/n_e)^{C_6}]}, \quad (\text{A.2})$$

where G_{FUV} represents the FUV fields measured in unit of the equivalent average interstellar radiation flux of $1.6 \times 10^{-3} \text{ erg cm}^{-2} \text{ s}^{-1}$ (Habing 1968), and T , n_{tot} , and n_e represent the gas temperature, the number densities of hydrogen nuclei and electrons, respectively. The parameter set of C_0 – C_6 is taken from Weingartner & Draine (2001b), where we choose the dust size distribution model for dense clouds with the ratio of visual extinction to reddening of $R_V \equiv A(V)/E(B-V) = 5.5$, the total C abundance per H nucleus in the log-normal population of $b_C = 3.0 \times 10^{-5}$, and the grain volumes assumed to be the same as those of the diffuse interstellar medium (case B of WD01a; see also Appendix D).

A.2. Gas–grain collisions

The energy exchange between gas and dust particles through collisions is one of the most important thermal processes in protoplanetary disks in which the density is high enough. We use the following cooling rate (heating rate if $T_d > T$) in this paper,

$$\Lambda_{\text{gr}} = 3.5 \times 10^{-34} n_{\text{tot}}^2 T^{0.5} (T - T_d) \text{ erg cm}^{-3} \text{ s}^{-1} \quad (\text{A.3})$$

(Burke & Hollenbach 1983; Tielens & Hollenbach 1985). The dust temperature T_d is obtained on the assumption of the local radiative equilibrium in Sect. 2.1.

A.3. Radiative cooling

Radiative transitions among the fine-structure levels of OI (63 μm) and CII (158 μm), and the rotational line transitions of CO contribute to cooling gas in the surface layer of the disks where the gas density is low enough. The cooling rate due to the transition from upper level i to lower level j of species s is calculated as

$$\Lambda_s(\nu_{ij}) = h\nu_{ij} \beta_{\text{esc}}(\tau_{ij}) \times [n_i \{A_{ij} + B_{ij} P(\nu_{ij})\} - n_j B_{ji} P(\nu_{ij})], \quad (\text{A.4})$$

where n_i , A_{ij} , B_{ij} , and $h\nu_{ij}$ are the population density of level i , the Einstein probabilities for spontaneous and stimulated emission, and the energy difference between levels i and j , respectively (e.g., de Jong et al. 1980). As the photon escape probability, $\beta_{\text{esc}}(\tau_{ij})$, we use the approximate function given by de Jong et al. (1980). Assuming that the nearest boundary from a point (r, z) is the disk surface (r, z_∞) , we approximately calculate the optical depth averaged over the line, τ_{ij} , as

$$\tau_{ij}(z) = \frac{A_{ij} c^3}{8\pi \nu_{ij}^3} \int_z^{z_\infty} n_i(z') \left[\frac{n_j(z') g_i}{n_i(z') g_j} - 1 \right] \frac{dz'}{\delta v_d(z')} \quad (\text{A.5})$$

$$\approx \frac{A_{ij} c^3}{8\pi \nu_{ij}^3} \frac{n_i(z)}{n_H(z)} \left[\frac{n_j(z) g_i}{n_i(z) g_j} - 1 \right] \frac{N_H(z)}{\delta v_d(z)}, \quad (\text{A.6})$$

where g_i is the statistical weight factors of the level i , $\delta v_d(z) = \{2kT(z)/\mu m\}^{0.5}$ is the Doppler line width, and $N_H(z) = \int_z^{z_\infty} n_H(z') dz'$ is the column density of hydrogen nuclei from z to z_∞ . The background radiation $P(\nu_{ij})$ is calculated by assuming that it is contributed by the radiation from the central star and the infrared dust emission,

$$P(\nu_{ij}) = (1/8)(R/R_*)^2 B(\nu_{ij}, T_*) \exp[-\tau_{d,R}(\nu_{ij})] + (1/2) B(\nu_{ij}, T_d) \{1 - \exp[-\tau_{d,z}(\nu_{ij})]\}, \quad (\text{A.7})$$

where T_* and R_* are the temperature and the radius of the central star, respectively, and $\tau_{d,R}(\nu_{ij}) = \int_{R_*}^R \kappa_{\nu_{ij}} \rho dR$ and $\tau_{d,z}(\nu_{ij}) = \int_z^{z_\infty} \kappa_{\nu_{ij}} \rho dz$ are the optical depth in the radial and the vertical directions, respectively. The dust temperature T_d is obtained on the assumption of local radiative equilibrium, as discussed in Sect. 2.1.

The level populations of CII and OI are obtained by solving the equations of statistical equilibrium,

$$n_i \sum_{j \neq i} R_{ij} = \sum_{j \neq i} n_j R_{ji}, \quad (\text{A.8})$$

where

$$\begin{aligned} R_{ij} &= A_{ij} + B_{ij} P(\nu_{ij}) + C_{ij}, \quad i > j, \\ R_{ij} &= B_{ij} P(\nu_{ij}) + C_{ij}, \quad i < j. \end{aligned} \quad (\text{A.9})$$

The symbol C_{ij} represents the collisional transition rate. The collisional de-excitation rate coefficients are taken from Tielens & Hollenbach (1985), and the collisional excitation rates are calculated as $C_{ij} = C_{ji}(g_j/g_i) \exp(h\nu_{ij}/kT)$ ($i < j$). The level population of CO is assumed to be in LTE, which will overestimate the CO cooling rate when $n_H < 10^7 \text{ cm}^{-3}$ (cf. Kamp & van Zaaldehoff 2001). The abundances of OI, CII, and CO are calculated as is described in Appendix B.2.

Appendix B: Chemistry

B.1. Hydrogen photoionization

It is known that extreme UV photons with energy of $h\nu > 13.6 \text{ eV}$ are mainly consumed to photoionize atomic hydrogen. Thus, we simply consider that most hydrogen atoms are ionized if

$$\int_{R_*}^r \alpha_H n_{\text{tot}}^2 dr < \int_{\nu_{\text{EUV}}}^{\infty} \frac{F_{\nu,R}}{h\nu} d\nu, \quad (\text{B.1})$$

where $\alpha_{\text{H}} = 2.58 \times 10^{-13} \text{ cm}^3 \text{ s}^{-1}$ is the recombination coefficient for atomic hydrogen at 10^4 K , $F_{\nu,R}$ is the radiation flux from the central star in Eq. (6), and $h\nu_{\text{EUV}} \equiv 13.6 \text{ eV}$ (e.g., Osterbrock 1989; Hollenbach et al. 1994). The temperature of this ionized region is simply assumed to be $T = 10^4 \text{ K}$, since we are interested in the structure of non-ionized region and the temperature of this ionized surface layer does not affect the global structure of the disks very much.

B.2. Carbon and oxygen chemistry

In order to calculate the radiative cooling by C^+ , O and CO, we treat a very simple chemistry for carbon and oxygen, and calculate the abundances of these species. The total fractional abundances of carbon and oxygen with respect to hydrogen nuclei are assumed to be $x(\text{C}_{\text{tot}}) = x(\text{C}^+) + x(\text{C}) + x(\text{CO}) = 7.86 \times 10^{-5}$ and $x(\text{O}_{\text{tot}}) = x(\text{O}) + x(\text{CO}) = 1.8 \times 10^{-4}$, respectively. The number density of carbon monoxide is calculated using the following two chemical equilibrium:

$$k_0 n(\text{C}^+) n(\text{H}_2) = k_1 n(\text{CH}_x) n(\text{O}) + G_{\text{FUV}} \Gamma_{\text{CH}_x} n(\text{CH}_2) \quad (\text{B.2})$$

and

$$k_1 n(\text{CH}_x) n(\text{O}) = G_{\text{FUV}} \Gamma_{\text{CO}} n(\text{CO}), \quad (\text{B.3})$$

as

$$n(\text{CO}) = \frac{k_1 n(\text{CH}_x) n(\text{O})}{G_{\text{FUV}} \Gamma_{\text{CO}}} \quad (\text{B.4})$$

$$= \frac{k_1 n(\text{O})}{G_{\text{FUV}} \Gamma_{\text{CO}}} \frac{k_0 n(\text{C}^+) n(\text{H}_2)}{k_1 n(\text{O}) + G_{\text{FUV}} \Gamma_{\text{CH}_x}}, \quad (\text{B.5})$$

following Nelson & Langer (1997) (cf. Langer 1976), where $k_0 = 5 \times 10^{-16} \text{ cm}^3 \text{ s}^{-1}$ is the rate coefficient of the radiative association reaction $\text{C}^+ + \text{H}_2 \rightarrow \text{CH}_2^+ + h\nu$ and $k_1 = 5 \times 10^{-10} \text{ cm}^3 \text{ s}^{-1}$ is the rate coefficient of the reaction between the hydrocarbon radicals and atomic oxygen to form CO. The symbol G_{FUV} represents the UV radiation described in Sect. 2.2, and $\Gamma_{\text{CH}_x} = 5 \times 10^{-10} \text{ s}^{-1}$ and $\Gamma_{\text{CO}} = 10^{-10} \text{ s}^{-1}$ are the photodissociation rates of the hydrocarbon radicals and the carbon monoxide, respectively. More detailed chemistry should be solved in future (e.g., Aikawa et al. 2002; Markwick et al. 2002; Kamp & Dullemond 2004).

Appendix C: Central stellar radiation

Here we model the radiation from the T Tauri star by means of black body emission at an effective stellar temperature plus optically thin hydrogenic thermal bremsstrahlung emission at a higher temperature (e.g., Lago et al. 1984; Costa et al. 2000) and Ly α line emission (e.g., Hergzeg et al. 2002). The specific luminosity at a wavelength λ of the photospheric black body radiation is calculated as

$$L_{\lambda,\text{bb}} = 4\pi^2 R_*^2 B_{\lambda}(T_*), \quad (\text{C.1})$$

while the luminosity of the coronal hydrogenic thermal bremsstrahlung emission is computed as

$$L_{\lambda,\text{br}} \approx \eta_{\lambda,\text{br}} V, \quad (\text{C.2})$$

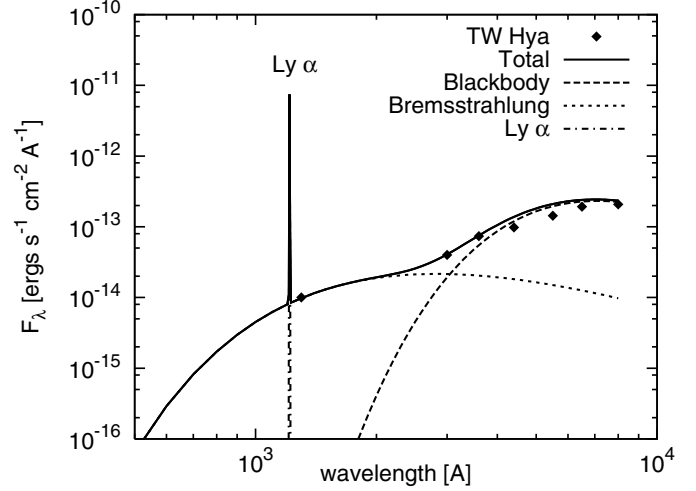


Fig. C.1. The radiation flux of the central T Tauri star (solid line) modeled by black body radiation (dashed line), thermal bremsstrahlung emission (dotted line), and Ly α line emission (dot-dashed line). The filled diamonds show the observational data towards TW Hya.

where V is the volume of the bremsstrahlung emission region and $\eta_{\lambda,\text{br}}$ is the emissivity,

$$\eta_{\lambda,\text{br}} = 2.0 \times 10^{-36} n_e^2 T_{\text{br}}^{-1/2} \lambda^{-2} \times \exp(-hc/\lambda k T_{\text{br}}) \text{ erg s}^{-1} \text{ cm}^{-3} \text{ \AA}^{-1}, \quad (\text{C.3})$$

(e.g., Rybicki & Lightman 1979). Here n_e , T_{br} , and c are the electron number density, the temperature of the bremsstrahlung emission, and the light speed, respectively. In addition, we take into account the luminosity of the Ly α line emission at the stellar surface,

$$L_{\lambda,\text{Ly}\alpha} = L_{\lambda_0,\text{Ly}\alpha} \exp[-(\lambda - \lambda_0)^2/\sigma^2], \quad (\text{C.4})$$

where we simply assume that the line has a Gaussian profile with the central wavelength of λ_0 , the peak luminosity of $L_{\lambda_0,\text{Ly}\alpha}$, and the line width of σ .

Now, we choose the physical parameters in Eqs. (C.2)–(C.4) by comparing the calculated radiation flux to observations towards TW Hya. The effective stellar temperature and radius of TW Hya of $T_* = 4000 \text{ K}$ and $R_* = 1 R_{\odot}$, and the distance to TW Hya of $d = 56 \text{ pc}$ are adopted in the calculation. Figure C.1 shows the calculated radiation flux density and the observational data. The dashed, dotted, dot-dashed, and solid lines represent the black body, the bremsstrahlung, the Ly α line, and the total radiation, respectively. The filled diamonds are the observations. The observational data at the *I*, *R*, *V*, *B*, and *U* bands are taken from Herbst et al. (1994). The median value of 11.02 mag is adopted for the *V* magnitude. The data of 2.0×10^{-14} and $1.0 \times 10^{-14} \text{ erg cm}^{-2} \text{ s}^{-1} \text{ \AA}^{-1}$ at the wavelengths of 1300 \AA and 3000 \AA , respectively, are measured from the observation by Costa et al. (2000). The best fit physical parameters of $T_{\text{br}} = 2.5 \times 10^4 \text{ K}$ and $n_e^2 V = 3.68 \times 10^{56} \text{ cm}^{-3}$ are obtained for the thermal bremsstrahlung emission. We note that according to the analysis of the IUE data towards pre-main-sequence stars by Johns-Krull et al. (2000), many classical T Tauri stars have color temperatures of $\sim 10^4 \text{ K}$, derived from the mean

continuum flux at the wavelengths of 1958 Å and 1760 Å, independent of the effective stellar temperatures. For the Ly α line emission, we adopt the central wavelength of $\lambda_0 = 1215.67$ Å, the luminosity ratio of the line peak to the continuum radiation of $L_{\lambda_0, \text{Ly}\alpha} / (L_{\lambda_0, \text{bb}} + L_{\lambda_0, \text{br}}) = 10^3$, and the line width of $\sigma = 2.01$ Å, following Herczeg et al. (2002; see also Ardila et al. 2002).

The radiation flux from the central star is calculated as $F_{\lambda, \text{star}} = (L_{\lambda, \text{bb}} + L_{\lambda, \text{br}} + L_{\lambda, \text{Ly}\alpha}) / (4\pi R_*^2)$ and $F_{\lambda, \text{star}} = L_{\lambda, \text{bb}} / (4\pi R_*^2)$ for the models with and without UV excess radiation, respectively. We note that $F_{\nu, \text{star}}$ in Sect. 2.2 is related to $F_{\lambda, \text{star}}$ as $\lambda F_{\lambda, \text{star}} = \nu F_{\nu, \text{star}}$, where ν is the frequency. In this paper we adopt the physical parameters of T_* , T_{br} , λ_0 , $L_{\lambda_0, \text{Ly}\alpha} / (L_{\lambda_0, \text{bb}} + L_{\lambda_0, \text{br}})$, and σ as mentioned above, and set the stellar radius to be $2 R_\odot$ for calculating the radiation from the central star, that is, we take the luminosity of the central star ($L_* = 4\pi R_*^2 F_*$) to be four times larger than that of TW Hya.

Appendix D: Grain opacity

In order to calculate the absorption (κ_ν) and scattering (σ_ν) coefficients of dust grains, we use the following dust model in this paper. First, as the dust components we adopt silicate and carbonaceous grains, both of which are considered as components of interstellar dust, and water ice, which is expected to be formed in the cold and dense region of protoplanetary disks. The optical properties of the carbonaceous grains are assumed to have a continuous distribution of graphite-like properties for larger sizes and PAH-like properties in the small size limit, following Li & Draine (2001). The mass fractional abundances of the above species are taken to be consistent with the solar elemental abundances: $\zeta_{\text{sil}} = 0.0043$, $\zeta_{\text{carbon}} = 0.0030$, and $\zeta_{\text{ice}} = 0.0094$ (Anders & Grevesse 1989). Their bulk densities are set to be $\rho_{\text{sil}} = 3.5$, $\rho_{\text{graphite}} = 2.24$, and $\rho_{\text{ice}} = 0.92$ g cm $^{-3}$ (see Li & Draine 2001 for the PAH's bulk density). Their sublimation temperatures are simply assumed to be $T_{\text{sil}} = 1500$ K, $T_{\text{carbon}} = 2300$ K, and $T_{\text{ice}} = 150$ K (e.g., Adams & Shu 1986).

We assume that the silicate and carbonaceous grain particles have the size distribution obtained by WD01a, which can reproduce the observational extinction curve of dense clouds with the ratio of visual extinction to reddening $R_V \equiv A(V)/E(B - V) = 5.5$ (see also Cardelli et al. 1989). We use the model with the parameter of $b_C = 3.0 \times 10^{-5}$, which represents the total C abundance per H nucleus in the log-normal population, and the grain volumes are assumed to be the same as those of the diffuse interstellar medium (case B of WD01a). The water ice is simply assumed to have the MRN size distribution of $dn/da \propto a^{-3.5}$, where a is the radius of the dust particles (Mathis et al. 1977).

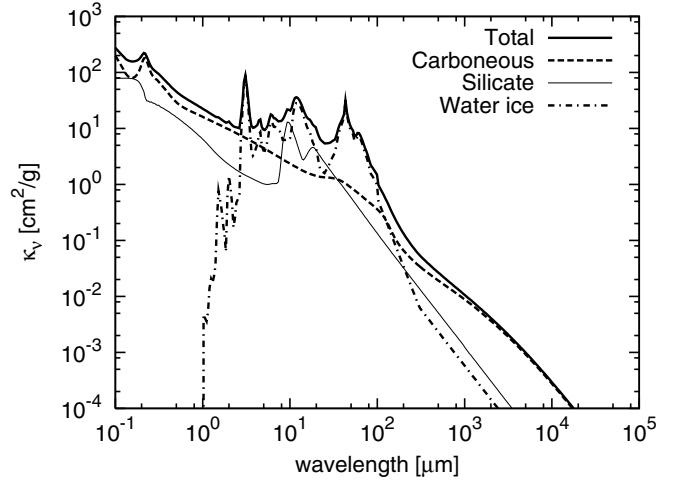


Fig. D.1. The monochromatic absorption coefficient (thick solid line) of dust grains consisting of carbonaceous (dashed line), silicate (thin solid line), and water ice (dot-dashed line).

The total mass absorption coefficient κ_ν and the total mass scattering coefficient σ_ν are calculated as

$$\{\kappa_\nu, \sigma_\nu\} = \sum_s \frac{\int (dn/da)_s a^3 \{\kappa_{\nu, s}(a), \sigma_{\nu, s}(a)\} da}{\int (dn/da)_s a^3 da}, \quad (\text{D.1})$$

where s represents the dust component – silicate, carbonaceous, or water ice. The mass absorption and scattering coefficients of dust particles with radius a is given by

$$\{\kappa_{\nu, s}(a), \sigma_{\nu, s}(a)\} = \frac{3}{4a\rho_s} \{Q_{\text{abs}}(a, \nu), Q_{\text{sca}}(a, \nu)\} \zeta_s \quad (\text{D.2})$$

(e.g., Miyake & Nakagawa 1993). We adopt the absorption factors $Q_{\text{abs}}(a, \nu)$ described in Li & Draine (2001) for PAH molecules. The other absorption and scattering efficiency factors, $Q_{\text{abs}}(a, \nu)$ and $Q_{\text{sca}}(a, \nu)$, are computed by means of the Mie theory (Bohren & Huffman 1983), simply assuming spherical grains. In order to calculate the efficiency factors, we use the dielectric function of the “smoothed UV astronomical silicate” and graphite by Draine & Lee (1984), Laor & Draine (1993), and WD01a (<http://www.astro.princeton.edu/~draine>). Also we use the refractive indices by Miyake & Nakagawa (1993, see also references therein) for the water ice.

The calculated monochromatic absorption coefficient is shown by the thick solid line in Fig. D.1. Each component of carbonaceous, silicate, and water ice is also plotted in the dashed, thin solid, and dot-dashed lines, respectively.